LTP induction drives remodeling of astroglia to boost glutamate escape from synapses

Christian Henneberger*&[1,2,9], Lucie Bard*[1], Aude Panatier*[3,4], James P. Reynolds*[1], Nikolay I. Medvedev*[5], Daniel Minge*[2], Michel K. Herde[2], Stefanie Anders[2], Igor Kraev[5], Janosch P. Heller[1], Olga Kopach[1], Sylvain Rama[1], Kaiyu Zheng[1], Thomas P. Jensen[1], Inmaculada Sanchez-Romero[6], Harald Janovjak[6], Ole Petter Ottersen[7], Erlend Arnulf Nagelhus[7], Stephane H.R. Oliet[3,4], Michael G. Stewart&[5], U. Valentin Nägerl&[4,8], Dmitri A. Rusakov&[1]

[1] UCL Institute of Neurology, University College London, UK

[2] Institute of Cellular Neurosciences, University of Bonn, Germany

[3] Inserm U1215, Neurocentre Magendie, Bordeaux, France

[4] Université de Bordeaux, Bordeaux, France

[5] Life Sciences, The Open University, Milton Keynes, UK

[6] Institute of Science and Technology Austria (IST Austria), 3400 Klosterneuburg, Austria

[7] Institute of Basic Medical Sciences, University of Oslo, 0317 Oslo, Norway

[8] Interdisciplinary Institute for Neuroscience, CNRS UMR 5297, Bordeaux, France

[9] German Center for Neurodegenerative Diseases (DZNE), Bonn, Germany

* Equal contribution / shared first authorship,

& Corresponding authors

Summary

Astroglia constrain extrasynaptic escape of the excitatory neurotransmitter glutamate, thus controlling synaptic signal integration in cortical circuits, which ultimately influences cognitive function. Memory formation is associated with synaptic remodeling but how the latter affects perisynaptic astroglia and thus extrasynaptic glutamate actions remains unknown. We used light diffraction-insensitive microscopy methods to find that a classical synaptic memory event, long-term potentiation (LTP), *ex vivo* and *in vivo*, at multiple or individual connections, triggers sub-microscopic withdrawal of astroglia from potentiated synapses. Molecular localization super-resolution imaging and optical glutamate sensors combined with patch-clamp reveal that LTP induction prompts spatial retreat of glial glutamate transporters, boosting glutamate spillover and thus NMDA receptor-mediated inter-synaptic signaling. The LTP-triggered shape change does not depend on major Ca^{2+}-dependent cascades in astrocytes but involves their NKCC1 transporters and the actin-controlling protein cofilin. Thus, a plasticity event at individual synapses engages an astroglial mechanism regulating excitatory signal integration among neighboring connections.

INTRODUCTION

Cell membranes of brain astroglia are densely packed with high-affinity transporters which rapidly take up glutamate released by excitatory synapses (Danbolt, 2001). Perisynaptic astroglial processes (PAPs) often occur in the close proximity of the synaptic cleft (Grosche et al., 1999; Heller and Rusakov, 2015; Ventura and Harris, 1999) to ensure that in most cases released glutamate activates immediate synaptic receptors rather than receptor targets on neighboring cell compartments including other synapses. However, a significant physiological impact of varied, astroglia-dependent extrasynaptic glutamate escape, or 'spillover', has long been acknowledged (Diamond, 2002; Kullmann and Asztely, 1998; Rusakov et al., 1999). In the hippocampus, glutamate spillover has been causally implicated in a co-operative action (including 'priming') of dendritic NMDA receptors (NMDARs) (Chalifoux and Carter, 2011; Hires et al., 2008), functional inter-synaptic cross-talk (Arnth-Jensen et al., 2002; Lozovaya et al., 1999; Scimemi et al., 2004), heterosynaptic potentiation and depression (Vogt and Nicoll, 1999), and remote activation of metabotropic glutamate receptors (Min et al., 1998; Scanziani et al., 1997), among other prominent phenomena. Escaping glutamate provides direct signaling between mitral cells in the olfactory bulb (Isaacson, 1999), and between climbing fibers and interneurons (Coddington et al., 2013; Szapiro and Barbour, 2007) as well as between parallel fibers and stellate cells (Carter and Regehr, 2000) in the cerebellum. At the behavioral level, a causative relationship has been demonstrated between changes in the astroglia-dependent glutamate escape and cognitive decline (Pereira et al., 2014), fear conditioning behavior (Tanaka et al., 2013; Tsvetkov et al., 2004), heroin and cocaine relapse (Shen et al., 2014; Smith et al., 2017), among other effects. Whether and how the degree of astrocyte-controlled glutamate spillover is regulated by neural activity has however remained an enigma.

Astrocytes have also emerged as a source of molecular signals that regulate synaptic transmission (Jourdain et al., 2007; Navarrete and Araque, 2010; Pascual et al., 2005; Santello et al., 2011) and contribute to the long-term modifications of synaptic circuitry associated with memory formation (Adamsky et al., 2018; Henneberger et al., 2010; Min and Nevian, 2012; Shigetomi et al., 2013). Again, molecular exchange between astrocytes and synapses is thought to rely in large part on the occurrence and function of nanoscopic PAPs (Panatier et al., 2006; Panatier et al., 2011). It has been therefore a long-standing question of whether PAPs undergo activity-dependent plastic changes that may in turn impact on the functioning of activated or nearby synapses. Addressing this question has been a challenge because the nanoscopic dimensions of PAPs are beyond the diffraction limit of conventional optical microscopy making it difficult to faithfully track their changes in live tissue.

Electron microscopy (EM) studies in fixed tissue have reported increased astroglial coverage of synapses in samples that underwent induction of synaptic long-term potentiation (LTP) (Bernardinelli et al., 2014; Lushnikova et al., 2009; Wenzel et al., 1991). An increase in the PAP occurrence has also been found in animals reared in complex environment (Jones and Greenough, 1996). In contrast, synaptic coverage by PAPs decreased following some memory consolidation tasks (Ostroff et al., 2014) or upon experiencing a lactation period (Oliet et al., 2001). However, EM cannot follow real-time physiological events and could be susceptible to distortions of astroglial morphology due to tissue fixation, including the appearance of spurious PAP shapes (Korogod et al., 2015). These factors necessitate complementary evidence in live cells. Several elegant studies have used fluorescence confocal or two-photon excitation (2PE) microscopy to monitor fine changes in the astroglial architecture (Bernardinelli et al., 2014; Haber et al., 2006; Hirrlinger et al., 2004; Perez-Alvarez et al., 2014). However, alterations in fluorescent shapes detected with conventional microscopy could be difficult to interpret, for

several reasons. Firstly, the size of and the separation between astrocyte processes are beyond the light diffraction limit, potentially giving rise to spurious structures, such as multiple neighboring PAPs appearing as one merged compartment (Rusakov, 2015). Secondly, commonly used bulk-loaded cell-permeable fluorescent tracers appear to underrepresent astroglial structure when compared to whole-cell loaded soluble intracellular dyes (Reeves et al., 2011). Importantly, local concentration changes or photobleaching of the fluorescent label could be mistaken for genuine morphological changes.

To avoid such uncertainties, we induced classical LTP in acute hippocampal slices and through sensory stimulation in the barrel cortex *in vivo* while monitoring local astroglia using several independent microscopy methods that are not limited by diffraction of light. We designed the experiments to examine synaptic populations with bulk-induced LTP as well as individual potentiated synapses. The results were internally consistent throughout pointing to a robust change in the local occurrence of PAPs and their glial glutamate transporters following LTP induction. We probed multiple astrocytic signaling cascades that might underlie the LTP-associated morphological plasticity of PAPs, and identified key protagonists. We then used two different optical glutamate sensors and a two-pathway electrophysiological test to determine whether the LTP-associated change in PAPs affects extrasynaptic glutamate escape. Our findings reveal that induction of synaptic plasticity triggers a rapid change in astroglial coverage of potentiated synapses, thus altering the degree of cross-talk among neighboring connections through glutamate spillover. This unexpected cell-signaling mechanism has a wide-ranging impact on excitatory signal integration in local circuitry and ultimately higher brain function. The newly discovered molecular machinery underpinning the LTP-triggered morphing of astroglia also unveils how certain patterns of neural activity could lead to astroglial morphogenesis.

RESULTS

LTP induction reduces tissue volume fraction occupied by local PAPs

In acute hippocampal slices, we imaged CA1 *stratum radiatum* astrocytes by loading them with the soluble fluorescent indicator Alexa Fluor 594 (or in some tests Texas Red Dextran; Method Details). In these settings, the fluorescence intensity collected within a thin two-photon excitation layer is proportional to the tissue volume fraction (VF) occupied by all local astroglial structures (Fig. 1A, *left*) as no other astrocytes occur within the same territory (Bushong et al., 2002). Furthermore, relating local astroglial fluorescence to its somatic fluorescence (100% VF) provides absolute VF values (Fig. 1A, *right*; Fig. S1A-B), as demonstrated earlier (Medvedev et al., 2014; Savtchenko et al., 2018). The average astroglial VF in the area was 6-7% (Fig. S1B-C; this excludes cell bodies). This value was similar to that obtained earlier in area CA1 (Savtchenko et al., 2018) and the *dentate gyrus* (Medvedev et al., 2014), and consistent with the earlier stereological EM data in CA1 neuropil (Lehre and Rusakov, 2002).

We therefore induced LTP at CA3-CA1 synapses using high-frequency stimulation of Schaffer collaterals (200-300 µm from the recorded astroglia) while monitoring astroglial VF and synaptic currents in the astrocyte proximity, as shown earlier (Henneberger et al., 2010) (Fig. 1B-C; Method Details). LTP induction prompted a progressive local VF decrease (up to 25-30%) lasting for at least 30 min (Fig. 1D). No such changes occurred in baseline conditions (Fig. 1D), confirming no concomitant effects of photobleaching. Interestingly, astroglial areas

with the smallest initial VF (i.e., where the thinnest processes occur) underwent the strongest VF reduction (Fig. 1E). We documented a qualitatively similar LTP-associated VF reduction when monitoring EGFP expressing astroglia (but found no detectable effects upon induction of long-term depression in similar settings; Fig. S1D-E).

The VF decrease was blocked when LTP induction was suppressed using either an NMDAR antagonist or by clamping Ca^{2+} in the patched astrocyte, in otherwise similar settings (Fig. 1F). We could rescue both LTP and the VF reduction under intra-astrocyte Ca^{2+} clamp by adding the NMDAR co-agonist D-serine to the bath (10 µM, Fig. 1F), consistent with earlier findings (Adamsky et al., 2018; Henneberger et al., 2010). These tests suggested that the observed VF changes were specific to LTP induction rather than to the stimulation protocol *per se*.

LTP-induced reduction of PAPs detected with unbiased image segmentation measures

We next sought to evaluate the LTP-induced changes in fluorescence-labelled PAPs using an unsupervised image segmentation method that does not depend on fluorescence intensity or average VF. The method reports the maximal number of well-resolved (separable) image objects across all binary brightness thresholds (Fig. 1G), providing a measure of structural partitioning or granularity, termed here 'segmentation'. The robustness of this measure was tested in *ad hoc* Monte Carlo experiment, in which we simulated ~4000 randomly oriented 3D nanoscopic astrocyte processes and plotted their z-axis projections inside a 2PE focal layer (Fig. S1F; Method Details). Throughout such tests, the segmentation measure decreased with greater sizes of simulated processes and increased with higher process numbers (Fig. S1G-H). Thus, an increase in segmentation should indicate larger numbers and/or smaller sizes of astroglial processes. Indeed, hypertonicity increased segmentation of the astrocyte images (Fig. 1H; Fig. S1I), reflecting shrunk (hence less overlapped and more separable) processes.

Importantly, the same osmotic challenge induced opposite changes in segmentation (Fig. 1H, grey bars) and in VF (Fig. 1F, grey bars), confirming the independence between the two measures. Following LTP induction, segmentation was reduced by 17 ± 7% (Fig. 1H). Theoretically, this should indicate either fewer nanoscopic processes or their increased size (or both); however, the net increase in size can be ruled out by the reduced VF post-induction (Fig. 1F). Therefore, the most parsimonious explanation for this finding is the withdrawal (or shrinkage beyond the detection limit) of smaller processes: in such a case, the average size of the remaining detectable processes would appear greater. We also found that another intensity-independent measure of the object heterogeneity, image entropy (Method Details), scaled sub-linearly with the astrocyte VF, both in experiments *in situ* and in Monte Carlo simulations (Fig. S1J). This measure decreased robustly following LTP induction (by 8.3 ± 2.1%, n = 18; $p < 0.001$; Fig. S1K), again pointing to a decrease in the PAP VF, in a brightness-insensitive manner.

LTP induction reduces diffusion connectivity among astroglial processes

Fluorescence recovery after photobleaching (FRAP) of a soluble intracellular indicator was previously used to gauge diffusion transfer along the nanoscopic necks of dendritic spines (Bloodgood and Sabatini, 2005; Svoboda et al., 1996). Earlier, we used a similar approach to monitor internal diffusion connectivity among astrocyte processes, by applying linescan FRAP in the middle of the astrocyte tree (Anders et al., 2014; Savtchenko et al., 2018) (Fig. 2A).

Here, we found that upon LTP induction, photobleaching was faster whereas recovery slower, with no such changes in control conditions (Fig. 2B-C). These results are consistent with the reduced connectivity among processes during LTP, possibly due to their partial shrinkage. At the same time, LTP induction had no detectable effect on the local extracellular diffusivity (Fig. 2C, right ordinate) as measured with the fluorescence point-source technique (Fig. S2A-C) described earlier (Zheng et al., 2008). This was not surprising because astroglia in area CA1 *stratum radiatum* occupy 6-7% of the tissue volume (Fig. S1C) (Savtchenko et al., 2018) of which 15-20% is taken by the extracellular space (Sykova and Nicholson, 2008). Hence, a 20-30% decrease in astroglial VF would add on average only 5-10% to the extracellular space volume, or 1-2% to the extracellular volume tissue fraction within the affected area.

Super-resolution STED imaging reports a decrease in the PAP presence near spines upon LTP induction

STED microscopy has been a powerful tool to monitor nanoscopic cellular compartments in live preparations, far beyond the optical diffraction limit (Tonnesen et al., 2018; Tonnesen et al., 2014). Here we turned to two-color STED imaging combined with electrophysiology in organotypic hippocampal slice cultures (Panatier et al., 2014) (Method Details). To image CA1 pyramidal cells and adjacent astroglia in two chromatically separated channels, we used the Thy1-YFP transgenic mice (neuron labelling) and held adjacent astrocytes in whole-cell mode loading them with Alexa Fluor 488.

We were thus able to monitor live dendritic spines of CA1 pyramidal neurons and local PAPs (resolution ~70 nm in *XY* plane) separately, before and after LTP induction, under unchanged imaging settings (Fig. 2D). To avoid any biased assessment of PAP changes, we once again employed volumetric readout, the ratio of green (astroglial) versus red (neuronal) pixels (*G/R* values) in the 1.5 µm proximity of individual spine heads (Fig. 2D). This ratio was decreased by 31 ± 10% following LTP induction ($n = 22$, $p < 0.001$), with no effect on red pixels that report dendritic structures (Fig. 2E). This result corroborates the reduced occurrence of PAPs, with no concomitant effects of photobleaching or dye escape in Thy1-YFP labelled structures. Similarly, any photobleaching in the astroglial channel was prevented by the continued dye dialysis.

The super-resolution images in the Thy1-YFP channel alone revealed subtle morphological changes in some dendritic spines during LTP (Fig. 2F, stars). To understand such changes in a greater detail, and also to minimize potential concomitants of STED-related photodamage during live monitoring of LTP, we also compared randomized groups of spines in control and potentiated slice preparations. We found that the fraction of spines occurring in close apposition to astroglia was reduced five-fold in the potentiated *versus* naive or control (APV presence) slices (Fig. 2G), consistent with the time-lapse experiments (Fig. 2D-E).

Intriguingly, spines dissociated from PAPs had a greater head size in the potentiated tissue compared to control conditions or NMDAR blockade (Fig. S2D-E). One interpretation of this observation is that PAPs near larger spines are more likely to undergo LTP-induced withdrawal, although there was no LTP-associated increase in the head size when averaged across all spines (Fig. S2D, *right*). Interestingly, potentiated tissue showed a greater fraction of distinctly large spine heads (>500 nm wide, 12/54) compared to control tissue (3/29) (Fig. S2D-E, *right*) whereas stimulated tissue under NMDAR blockade showed no such difference

(5/16). These observations suggest a complex picture of spine morphogenesis under the HFS-induction protocol, which would require a separate study.

Volumetric correlational 3D EM reports reduced occurrence of PAPs after LTP induction

In order to further characterize the nanoscale nature of the LTP-associated PAP changes we employed correlational quantitative 3D EM. We patched an astrocyte 15-20 min post LTP induction in the close proximity of the LTP-reporting microelectrode (as in Fig. 1B) and loaded it with biocytin (Fig. 3A). This was followed by rapid slice submersion into fixative and DAB conversion for EM identification (Fig. 3A-B; Method Details). The slices were cut into ultrathin (60-70 nm) sections and examined visually until the patched astrocyte (arrow in Fig. 3A) could be reached and identified (Fig. 3B). 200-300 contiguous serial sections were then used to reconstruct in 3D an astrocyte fragment of interest and the adjacent synapses, identified by their characteristic morphology and the presence of the postsynaptic density (PSD, Fig. 3C, Fig. S3A-B), as described previously (Medvedev et al., 2014; Savtchenko et al., 2018).

To evaluate the extent of synaptic PAP coverage in a shape-insensitive fashion, we calculated the VF occupied by PAPs inside 100 nm–wide concentric spherical shells centered at individual PSDs (Fig. 3D, Method Details). Thus, we obtained the distribution of PAP coverage up to a distance of ~0.5 µm from the synapse, which is the average nearest-neighbor distance between CA3-CA1 synapses (Rusakov and Kullmann, 1998). Given the different functional identities of 'thin' and 'mushroom' spines in CA1 pyramidal cells (Matsuzaki et al., 2001) we treated these two populations separately. This analysis indicated clear astroglial withdrawal (or shrinkage away from spines) following LTP induction, for both spine types (Fig. 3E, Fig. S3C). Furthermore, comparing 2PE live imaging and 3D EM data strongly argued that the EM results were unlikely to be biased by the possible deficiencies in EM tissue fixation (Korogod et al., 2015) (see Discussion for details).

dSTORM molecular maps relate LTP to larger distances between synapses and glial glutamate transporter GLT-1

Because astroglial membranes are packed with glial glutamate transporter GLT-1 (Danbolt, 2001), the LTP-associated withdrawal of PAPs suggests that the perisynaptic arrangement of GLT-1 could also change. To test whether this is the case, we set out to explore molecular localization of perisynaptic GLT-1 using super-resolution dSTORM technique as described previously (Heller et al., 2017), in control condition and after LTP induction. Aiming to potentiate the vast majority of synapses in the tissue, we turned to the classical chemically-induced LTP (cLTP) protocol in acute hippocampal slices (Otmakhov et al., 2004): electrophysiology confirmed robust LTP induction (Fig. S3D). Molecular mapping of presynaptic protein Bassoon and postsynaptic Homer1 was employed to delineate, respectively, presynaptic active zones and postsynaptic densities in three dimensions.

Three-color 3D dSTORM revealed a detailed spatial pattern for many hundreds of GLT-1 molecules occurring around individual synaptic contacts (Fig. 3F; Fig. S3E). Strikingly, in the potentiated tissue, GLT-1 were consistently registered at significantly larger distances from bassoon protein, a molecular partner of synaptic vesicle release (Fig. 3G; 23 and 43 synapses in five control and five potentiated preparations, respectively). This finding was consistent with

the withdrawal of PAPs upon LTP induction, suggesting that glutamate released from potentiated synapses has to travel, on average, greater distances before being picked by astroglial transporters.

Molecular protagonists of LTP-induced astroglial PAPs withdrawal

What are the cellular mechanisms underlying the LTP-induced astroglial VF reduction? First, we asked if a major astroglial Ca^{2+}-signaling cascade that engages metabotropic glutamate receptors (mGluRs) and IP_3 receptors (Porter and McCarthy, 1997; Volterra et al., 2014) and affects astrocyte process mobility (Perez-Alvarez et al., 2014) could be involved. We found that 2PE spot-uncaging of IP_3 inside astrocyte branches generated robust local Ca^{2+}-signals (Fig. 4A-B) yet neither this localized stimulus nor the pressure-puff pipette application of the wide-spectrum mGluR agonist DHGP had any effect on astroglial VF (Fig. 4C). Similarly, WIN55, an agonist of cannabinoid CB1 receptors, which contribute prominently to astroglial function (Navarrete and Araque, 2010) while inhibiting CA3-CA1 transmission (Sylantyev et al., 2013), had no detectable effect on VF (Fig. 4C). Nor did the $GABA_A$ receptor agonist muscimol whose action has recently been associated with a slight shrinkage of sulforhodamine-101 stained astroglia (Florence et al., 2012) (Fig. 4C).

We next tested the involvement of the known external morphogenic signals that could be invoked during LTP induction, such as the extracellular matrix (ECM) components (Dityatev and Schachner, 2003) and the ephrin/Eph-dependent molecular cascades attributed to astrocyte-dependent stabilization of dendritic compartments (Filosa et al., 2009; Murai et al., 2003; Nishida and Okabe, 2007). We therefore catalytically removed the key ECM component chondroitin sulfate with chondroitinase ABC (Kochlamazashvili et al., 2010) and blocked EphA4 activity with EphA4-Fc using a previously validated protocol (Filosa et al., 2009; Murai et al., 2003). These manipulations, however, had no effect on LTP induction or the consequent reduction of astroglial VF (Fig. 4D).

We next turned to the astroglial morphogenic mechanisms associated with cell ion and water exchange, in which aquaporin-4 (AQP4) plays a prominent role (Nagelhus and Ottersen, 2013). To test the role of AQP4 we carried out experiments in AQP4 KO mice (Thrane et al., 2011) and, surprisingly, found that LTP induction and the associated reduction in astroglial VF were intact (Fig. 4D-E). Another key player in astrocyte volume regulation is the Na^+-K^+-$2Cl^-$ cotransporter NKCC1 widely expressed in astroglia (Hoffmann et al., 2009; Kaila et al., 2014). To test its role in a cell-specific manner, we dialyzed individual recorded astrocytes with the NKCC1 blocker bumetanide (20 µM) through the whole-cell patch pipette. Strikingly, this intracellular bumetanide action blocked VF changes while preserving LTP induction (Fig. 4D-E). This result was confirmed in rats with 50 µM intracellular bumetanide, showing intact LTP-associated VF reduction against the control experiment with the vehicle DMSO (Fig. 4D-E; in the latter tests, 100 µM AQP4 blocker TGN-020 (Igarashi et al., 2011) was also added to bath medium, to approach conditions of AQP4 KO, although the TGN-020 efficiency has recently been challenged (Tradtrantip et al., 2017)). We have also confirmed that bumetanide (or its vehicle DMSO) had on its own no effect on the astroglial volume (Fig. S4A). Thus, LTP-induced astroglial withdrawal specifically requires action of NKCC1.

What could be the downstream signal of NKCC1? It has recently been proposed that NKCC1 (characteristic of astroglia) serves as a protein scaffold regulating, in a pH-sensitive fashion, the phosphorylation of a small (19 kDa) freely-diffusible protein cofilin-1 (Schiapparelli et al.,

2017), and that the ion transporter KCC2 drives a similar cascade in neurons (Llano et al., 2015). Cofilin-1 is a well-established bi-directional regulator of actin filament polymerization, which is directly related to cell protrusion formation and retrieval, such as dendritic spine morphogenesis (Bravo-Cordero et al., 2013; Ethell and Pasquale, 2005). To test whether this signaling cascade is involved in the LTP-induced astroglial withdrawal, we dialyzed astrocytes, via the whole-cell pipette, with an intracellular solution containing peptide S3 (Liu et al., 2016), which inhibits phosphorylation of cofilin-1 (Aizawa et al., 2001) (Method Details).

Surprisingly, peptide S3 dialysis triggered astroglial shrinkage by 20-30%, with the range and dynamics akin to that seen during LTP induction in similar settings but without peptide S3 (Fig. 4D-E; in the same experiment, astroglia connected to the patched cells via gap junctions, which are impermeable for peptide S3, showed perfectly stable VF values). Importantly, when we induced LTP near astrocytes dialyzed with peptide S3 (here LTP expression was similar to that in control, Fig. S4B-D), PAP shrinkage was indistinguishable from that during control-condition LTP or during the peptide S3 dialysis without LTP (Fig. 4D-E). Thus, interference with cofilin-1 activity fully occluded the effect of LTP induction, indicating the common molecular underpinning. These tests thus unveil key molecular players in the cellular cascades that relate the induction of LTP at excitatory synapses with the withdrawal of local PAPs (Fig. 4F, see Discussion).

Single-synapse LTP induction prompts retraction of adjacent PAPs

Whilst the above tests consistently point towards the same robust phenomenon, they have a common shortcoming: potentiated tissue may contain a mixture of potentiated and non-potentiated or inactive synapses, thus potentially introducing a bias. We therefore sought to induce LTP at individual identified synapses while monitoring the adjacent astroglia. Glutamate spot-uncaging has classically been used to induce LTP at individual CA3-CA1 synapses (Harvey and Svoboda, 2007; Matsuzaki et al., 2004; Yasuda et al., 2003). Here, we implemented a modified protocol in which the postsynaptic cell is unclamped while the spot-uncaging follows the standard HFS-induction regime: this arrangement is in keeping with the classical protocol used elsewhere in the present study.

First, we held the postsynaptic CA1 pyramidal cell in voltage clamp, visualized a dendritic spine, and positioned the laser uncaging spot near it (Fig. 5A, Fig. S5A; Method Details). Next, we adjusted laser power (two-photon uncaging) so that individual 1 ms light pulses could induce EPSC waveforms akin to those evoked by minimal stimulation in similar settings (Rusakov and Fine, 2003) (Fig. 5B). Second, we switched to current clamp while maintaining V_m at -60 to -65 mV, similar to that in freely-moving animals (Epsztein et al., 2010). Next, we applied the spot-uncaging sequence replicating the HFS induction protocol. This induced robust postsynaptic Ca^{2+} entry (Fig. S5A-B), confirming suitable conditions for LTP induction. After the induction protocol, we switched back to voltage clamp and resumed recording single-pulse EPSCs under baseline conditions (Fig. 5B). In these experiments, potentiation was robustly induced at every sampled synapse (7 out of 7 cells, Fig. 5B-C).

Because CA3-CA1 synapses are only half a micron apart (Rusakov and Kullmann, 1998), our spot-uncaging protocol (Fig. 5A-B) should potentiate at least one synapse nearby, whether or not the unclamped postsynaptic cell is visualized. We therefore applied this protocol in *stratum radiatum* while monitoring astroglial VF and Ca^{2+} in the proximity of the uncaging spot (Fig. 5D). The LTP-inducing uncaging sequence in most cases (11 out of 14) evoked a detectable

local Ca^{2+} response in astroglia (Fig. 5D-E, Fig. S5E). In such cases, it also induced a progressive VF reduction in PAPs near the spot (Fig. 5F-G; Fig. S5C-D). No detectable VF changes were found either in 'remote' areas (>3 µm away from the spot), or when the protocol was applied without MNI-glutamate (Fig. 5G-H). Importantly, the blockade of astroglial NKCC1 with intracellular bumetanide completely blocked the LTP-associated reduction of VF (Fig. 5H).

Monitoring astroglia near active synapses *in vivo* during LTP induction

Whilst the above data (Fig. 5) provide evidence at a single-synapse level that LTP induction causes withdrawal of local PAPs, it was important to test our basic observations in a living animal. Building upon our earlier *in vivo* imaging protocols (Mishra et al., 2016; Savtchenko et al., 2018; Zheng et al., 2015), we used viral transduction to express (hSyn) GCaMP6f in the ventral posteromedial nucleus (VPM) that sends axonal projections to the barrel cortex (Fig. 6A), whereas cortical astroglia were transduced to express (GfaABC1D) tdTomato (Fig. 6B). This arrangement enabled us to monitor, through a cranial window implanted over the barrel cortex (layer *II/III*; Fig. 6B,D) of lightly anaesthetized mice, local astroglia as well as Ca^{2+} activity in individual axonal boutons that respond to contralateral rhythmic whisker stimulation (RWS; Fig. 6D).

Once we identified an axon that trespasses the territory of an individual astrocyte, we confirmed that a short RWS train induced clearly detectable Ca^{2+} elevations in its presynaptic boutons (Fig. 6E-F) and that local astroglial VF readout was similar to that in our whole-cell measurements (Fig. 6G). We next monitored astroglial VF near active axonal boutons and applied an established physiological protocol of RWS-induced LTP in this barrel cortex area (Gambino et al., 2014; Megevand et al., 2009) (3 Hz air stimuli, 100 ms pulse width, for 120 s, Fig. 6C). We found that LTP induction leads to a reduction in local astroglial VF. Astroglia showed no VF changes when RWS was performed on the ipsilateral whiskers (Fig. 6H-I).

We took advantage of similar imaging settings to further improve physiological relevance of our LTP protocols in acute hippocampal slices. We filled a CA3 pyramidal cell with the Ca^{2+} indicator OGB-1 and traced its axon into area CA1 populated with tdTomato-expressing astrocytes (Fig. S6A-B). We then paired presynaptic spikes with the postsynaptic depolarization of CA1 pyramidal cells (using the extracellular electrode placed in *s. pyramidale*), thus engaging one of the classical LTP induction protocols (Fig. S6C-D). Monitoring astroglial VF near activated axonal boutons revealed an LTP-associated VF reduction of 12 ± 2% (n = 5), which was not detected in areas devoid of the firing axon (3.4 ± 1%, n = 10; difference at $p < 0.01$; Fig. S6E).

LTP-induced PAP withdrawal boosts local extrasynaptic glutamate escape detected with optical sensors

To test whether LTP-associated withdrawal of PAPs and the retreat of GLT-1 (detected with dSTORM) indeed alter extrasynaptic glutamate escape, we carried out two complementing experiments. In the first experiment, we used the optical glutamate sensor FLIPE600n (Okumoto et al., 2005) modified for sensor immobilization in the extracellular space (Okubo et al., 2010), as described previously (Whitfield et al., 2015) (Fig. 7A, Fig. S7A; Method details). The sensor was highly sensitive to glutamate *in vitro* and *in situ* (Fig. S7B) and could be

delivered to CA1 *stratum radiatum* using a patch pipette (Fig. 7A-B). Burst stimulation of Schaffer collaterals induced a clear, stimulus strength-dependent optical response (Fig. 7C, Fig. S7C). In these settings, LTP induction (Fig. 7D) was accompanied by a substantial increase in the bFLIPE600n response (Fig. 7E). This suggested a greater exposure of bFLIPE600n to an extracellular (extrasynaptic) glutamate transient after LTP induction, even though LTP does not increase the amount of glutamate released (Diamond et al., 1998; Luscher et al., 1998), as we confirmed below.

In the second experiment, we expressed the glutamate sensor iGluSnFR (Marvin et al., 2013) on the outer surface of either astroglial or neuronal membranes in hippocampal area CA1 (Fig. S7D; Method Details). The iGluSnFR signal faithfully reported local synaptic responses (Fig. S7E) including their paired-pulse ratios (Fig. S7F-G): the latter was not affected by LTP induction (Fig. S7G) pointing to unchanged release probability, as expected. We therefore used iGluSnFR imaging to probe glutamate escape near individual potentiated synapses.

We held a CA1 pyramidal cell (Fig. 7F) or an astrocyte (Fig. S7H-I), and applied individual spot-uncaging pulses as described above (Fig. 5A-B), either in the vicinity of the dendritic spine or in the astrocyte territory (red channel) while monitoring local iGluSnFR activation by glutamate with linescan imaging (green channel, Fig. 7G *top*). Next, we applied the spot-uncaging LTP induction protocol and 10-30 min later repeated single-pulse uncaging while collecting iGluSnFR profiles (Fig. 7G *bottom*). We found that LTP induction widened the spatial spread of the glutamate signal (Fig. 7H-I; n = 12). Importantly, the glutamate escape was unaffected by LTP induction when we dialyzed local astroglia (Fig. S7H-I) with the NKCC1 blocker bumetanide (20 µM; Fig. 7I; Fig. S7J-K). These results lend independent support to the hypothesis that LTP induction boosts extrasynaptic glutamate escape, following local withdrawal of PAPs.

LTP induction prompts 'sharing' of NMDARs among excitatory synapses

If LTP induction enhances extrasynaptic glutamate escape it may also boost activation of extrasynaptic high-affinity glutamate receptors, such as NMDARs, including receptors at the neighboring synapses. It has been established in multiple studies that this could have fundamental implications for synaptic signal integration in local circuitry and ultimately for cognition and behavior (see Introduction). To test directly whether such a mechanism indeed acts in our case, we implemented a previously validated protocol to monitor NMDAR-mediated cross-talk between two independent Schaffer collateral pathways (Scimemi et al., 2004) (Fig. S8A; Method Details).

This protocol takes advantage of the use-dependent NMDAR inhibitor MK801, which blocks the receptor only upon its activation. Thus, if NMDARs at non-active synapses appear blocked in the presence of MK801 over a period of time these receptors must have been activated by glutamate escaping from activated synapses nearby. Therefore, after recording baseline AMPA receptor-mediated EPSCs (AMPAR EPSCs) and then NMDAR EPSCs in both pathways, we applied MK801 to document progressive NMDAR EPSC inhibition while stimulating only one (control) pathway while keeping the other pathway silent (Fig. 8A). When stimulation resumed in the silent pathway, its NMDAR EPSCs were close to their baseline amplitude (Fig. 8A, top dotted line; Fig. S8B, *no-LTP, test*). Thus, the silent pathway had little cross-activation of NMDARs by synaptic discharges in the control pathway.

This changed when we induced LTP in the control pathway prior to recording NMDAR EPSCs (Fig. 8B, left ordinate). Resuming stimulation of the silent pathway revealed significantly reduced NMDAR EPSCs (Fig. 8B, double headed arrow; Fig. S6B, *LTP*, *test*). Thus, a proportion of this pathway's NMDARs had been activated by glutamate escaping from synapses in the control pathway (see Discussion for quantitative estimates). LTP induction in both pathways produced a similar boost of NMDAR-dependent inter-pathway cross-talk (Fig. 8C, Fig. S8C). We confirmed that no appreciable changes in presynaptic release probability were detected here after LTP induction (Fig. S8D), consistent with earlier reports (Manabe and Nicoll, 1994).

Our findings thus point to an internally consistent scenario (Fig. 8D) in which LTP-associated withdrawal of PAPs boosts extrasynaptic glutamate escape, thus prompting activation of NMDARs further away from the release site, potentially involving neighboring synapses (Fig. 8D). Finally, to test how biophysically plausible this sequence of events is, we employed a detailed Monte-Carlo model of CA3-CA1 synapses (Fig. S8E) (Zheng et al., 2008) and simulated three 'competing' scenarios consistent with our empirical observations. In these scenarios, glutamate transporter-enriched PAPs either withdrew, lost some transporters, or moved laterally (Fig. S8F), thus partly exposing extrasynaptic NMDARs. The tests suggested that PAPs shrinkage and glutamate transporter retreat, but no changes in transporter numbers, was most likely to boost extrasynaptic NMDAR activation (Fig. S8G). The latter is in line with the most parsimonious explanation of our experimental findings.

DISCUSSION

LTP and plasticity of synaptic microenvironment

The present study set out to test the hypothesis that the classical paradigm of synaptic LTP not only boosts the transmission efficacy at the target excitatory synapse but also remodels astroglial synaptic environment thus changing the local rules of glutamate signaling. This hypothesis was prompted by numerous observations reporting important consequences of the variable degree of extrasynaptic glutamate escape (spillover) for neural signal propagation and integration in various brain circuits (Arnth-Jensen et al., 2002; Coddington et al., 2013; Isaacson, 1999; Schiller et al., 2000; Szapiro and Barbour, 2007; Vogt and Nicoll, 1999).

We therefore used several established protocols of LTP induction in hippocampal and cortical synapses, including sensory-stimulation induced LTP in the barrel cortex *in vivo*. To evaluate real-time changes in PAP morphology during LTP induction, we applied several independent methods of (diffraction-insensitive) live imaging which shared one important feature: individual astroglia were filled with a bright, soluble morphological indicator, either through whole-cell dialysis of a synthetic dye (Alexa Fluor 594) or via astroglia-specific expression of fluorescent proteins (such as EGFP and tdTomato). In these settings, we employed conventional 2PE microscopy and monitored PAP changes using morphological readout - the local tissue VF occupied by astroglia - which does not require the knowledge of the sub-diffraction shapes of PAPs. These tests were carried out both in the bulk of astroglial processes and in the vicinity of individual potentiated synapses. The results consistently indicated an LTP-associated reduction in the VF of PAPs, within 20-30 min post-induction.

This phenomenon was further examined using two independent imaging approaches that have access to the morphological information in living cells on the nanoscale. The 2PE FRAP gauged the internal connectivity among optically unresolvable processes, and STED

microscopy enabled direct visualization of neuronal dendrites and adjacent astroglia beyond the diffraction limit. Both methods produced results that were consistent with the reduced presence of PAPs following LTP induction.

3D EM: faithful representation of live tissue?

We also used correlational serial-section 3D EM to gauge PAP changes on the nanoscale in potentiated tissue. The suitability of EM analyses based on tissue fixation has recently been questioned in elegant comparative tests showing that chemical fixation *in vivo* may produce drastic shrinkage of cortical tissue (~18% linear shrinkage), in particular its extracellular space (from ~15% to ~2% tissue volume), leading to the corresponding spurious increases in synaptic density and astroglial synaptic coverage (Korogod et al., 2015). However, different chemical fixation protocols produce varied outcomes. Our earlier studies reported 5-6% linear tissue shrinkage upon fresh hippocampal slice fixation by submersion and subsequent embedding (Rusakov et al., 1998) whereas the EM-evaluated extracellular space fraction in area CA1 was ~12% (Rusakov and Kullmann, 1998), only slightly smaller than the 15% estimated in live tissue (Sykova and Nicholson, 2008). In chemically fixed CA1 tissue, astroglia occupied ~9% of tissue volume (Lehre and Rusakov, 2002), which if anything was slightly larger than the 5-10% (depending in the inclusion / exclusion of the soma and large primary processes) estimated in the present study using live VF imaging. Furthermore, in the correlational EM studies employing rapid hippocampal slice fixation, astroglial VF in the dentate gyrus was undistinguishable between fixed-tissue EM and live imaging data (both at ~8%) (Medvedev et al., 2014).

In the present work, we therefore used quantitative EM based on slice-fixed tissue, which was prepared identically for both control and potentiated samples. We found a clear decrease in the occurrence of PAPs near excitatory synapses 20-25 min after LTP induction, judging by the reduced perisynaptic distribution of astroglial VF. To avoid ambiguity, we made no attempts to assess PAP shapes or describe their exact position. This, in addition to the differences in the experimental protocol, might explain an apparent discrepancy with some previous studies: for instance, smaller-VF PAPs that occur closer to synapses might count as an increase in PAP occurrence (Lushnikova et al., 2009; Wenzel et al., 1991) even though their overall VF (and hence overall glutamate uptake capacity) should decrease.

Changes in perisynaptic GLT-1 patterns revealed by 3D dSTORM

The key advantage of super-resolution dSTORM imaging compared to 3D EM techniques is that it could reveal contiguous spatial patterns of molecular expression, at single-molecule resolution: the latter has not been feasible even when using well-preserved serial EM sections combined with immuno-gold labelling. Here we used 3D three-color dSTORM to find that in potentiated tissue glial glutamate transporters GLT-1 tend to occur further away from synapses than in control conditions. Thus, the LTP-triggered withdrawal of PAPs was paralleled by a partial 'retreat' of glutamate transporters. This conclusion should not depend on variations in the GLT-1 antibody binding efficiency among preparations because we specifically look into the spatial patterns, rather than expression levels, by normalizing molecule occurrences to the overall staining intensity. Clearly, a separate study would be required to see whether the absolute expression of GLT-1 changes upon LTP induction and whether LTP induction protocols other than 'chemical LTP' trigger similar changes. Nonetheless, this result was fully

consistent with the biophysical notion that astroglia (at least in area CA1) control extrasynaptic glutamate escape by providing powerful high-affinity uptake (mainly via GLT-1), rather than simply presenting a diffusion obstacle in the shape of PAPs (Zheng et al., 2008).

Cellular mechanisms underlying PAP withdrawal

First, we found that the withdrawal of perisynaptic astroglia following LTP induction depends on the ion exchanger NKCC1, which has been considered a key morphology regulator actively participating in brain cell migration (Garzon-Muvdi et al., 2012; Haas and Sontheimer, 2010). In glioma cells, it mediates hydrodynamic volume changes and thus prompts dramatic morphological transformations which enable migratory invasion of intact brain tissue (Watkins and Sontheimer, 2011). In these cells, NKCC1 activity can lead to a (local) accumulation of intracellular chloride of up to 140 mM triggering prominent cellular shrinkage, up to 35% (Habela et al., 2009). It has recently been discovered that in glioblastoma cells NKCC1 regulates phosphorylation of cofilin-1 (Schiapparelli et al., 2017). Whilst NKCC1 typically occurs in astrocytes, the neuron-specific ion transporter KCC2 has been known to also target cofilin-1 activity (Llano et al., 2015). The mechanism engaging cofilin-1 appears essential for controlling actin filament polymerization, and thus generation and retrieval of cell filopodia and other thin processes, such as dendritic spines in nerve cells (Bravo-Cordero et al., 2013; Ethell and Pasquale, 2005). We have found that interfering with cofilin-1 phosphorylation by dialyzing individual astrocytes with peptide S3 (Aizawa et al., 2001; Liu et al., 2016) completely occludes the LTP-induced shrinkage of astroglial processes such as PAPs. Thus, our results unveil an internally consistent molecular cascade, which could causally explain how the induction of the NMDA receptor -dependent synaptic potentiation could trigger structural changes in local PAPs.

In a wider context, this finding raises a highly intriguing question: can this mechanism act as a ubiquitous 'transponder' of neuronal activity into astrocyte morphogenesis? Intriguingly, the critical role of ion channels and transporters akin to NKCC1 in engaging morphological plasticity of brain cells (which often related to cell migration and invasion) has been rapidly emerging, albeit shown predominantly in cell culture systems (Schwab et al., 2012). Our results thus help to understand the underpinning cellular machinery acting in brain cells *in situ*.

The reduced presence of PAPs boosts extrasynaptic glutamate escape

Changes in PAP geometry on the nanoscale following LTP induction should not affect total glutamate uptake because all released glutamate molecules will still be rapidly bound and taken up by transporters in the same astrocyte, as was indeed demonstrated earlier (Diamond et al., 1998; Luscher et al., 1998). Because glutamate diffusion and transporter binding within <500 nm occur on the sub-millisecond scale, subtle astroglial rearrangement within such spaces should have no detectable effect on the overall uptake kinetics, especially if measured at the soma. Similarly, PAP withdrawal should not affect the local steady-state occupancy of NMDARs by their co-agonists D-serine and glycine released from astroglia (Henneberger et al., 2010): since the agonists face no known high-affinity extracellular buffers (apart from NMDARs themselves), the nanoscopic re-arrangement of PAPs should have little effect on their steady-state equilibration in the extracellular space. However, if changes in PAPs 'relocate' agonist release sites, the relative contribution of either agonist to the occupancy of local NMDARs could change (Panatier et al., 2006; Papouin et al., 2012).

Nonetheless, with the reduced PAP presence, glutamate should dwell a fraction longer and travel a fraction further in the extrasynaptic extracellular space before being taken up by astroglial transporters. This is precisely in line with the results reported by the extracellular optical glutamate sensor bFLIPE600n, which should bind glutamate before it reaches its transporters. A similar phenomenon was documented on the microscopic scale when we expressed the glutamate sensor iGluSnFR in CA1 pyramidal cells. The sensor reported broadened glutamate dispersion from its two-photon uncaging spot following an LTP induction protocol applied to the adjacent synapse. The observation that LTP induction leads to a greater transient exposure of glutamate to the extracellular space (rather than to a greater amount of released glutamate) might explain, at least in part, why some pioneering earlier studies reported increased extracellular glutamate responses detected with an extracellular dialysis micro-electrode during LTP (Bliss et al., 1986; Errington et al., 2003).

Importantly, because our observations were necessarily limited to 30-40 min after LTP induction, they do not preclude the possibility for astroglial synaptic coverage to re-establish itself on a longer time scale. Whether a plasticity event indeed triggers such a dynamic sequence of astroglial rearrangement remains an important question.

Inter-synaptic NMDAR 'sharing': quantitative estimates and physiological implications

We examined network implications of increased glutamate escape by evaluating NMDAR-mediated cross-talk between two independent afferent pathways converging onto the same CA1 pyramidal cell. After LTP induction, ~120 single stimuli applied to one pathway activated up to 40% of NMDARs in the other, silent pathway. At first glance, this suggests that a single release event activates a negligible fraction (<0.4%) of NMDARs at neighboring synapses. However, these experiments probe cross-talk among relatively sparse synapses because only 2-3% of CA3-CA1 synapses are activated in either pathway under this protocol (Scimemi et al., 2004). Because the nearest-neighbor inter-synaptic distance in this area is ~0.5 µm (Rusakov and Kullmann, 1998), 2% synapses will be separated by $0.5 \cdot (0.02^{-1/3})$ ~ 1.8 µm. Increasing the distance from a glutamate source from 0.5 µm to 1.8 µm will roughly correspond to a >100-fold concentration drop (over the first 0.5 ms post-release) (Rusakov, 2001; Zheng et al., 2008). Thus, the NMDAR-mediated cross-talk among 2% of synapses 'accumulated' over ~120 trials in our test should either be comparable with or underestimate the cross-talk between close synaptic neighbors following a single release event.

Our findings thus suggest a scenario in which LTP induction is followed by a withdrawal of PAPs, increased glutamate escape and, consequently, enhanced inter-synaptic cross-talk via NMDARs. Intriguingly, this result might explain the reduced NMDAR EPSC variability during LTP at CA3-CA1 synapses (Kullmann et al., 1996), an enhanced local excitability of pyramidal cell dendrites after LTP induction (Frick et al., 2004), and why LTP at one synapse could lower the NMDAR-dependent LTP induction threshold at the neighbor (Harvey and Svoboda, 2007). Among other important functional consequences of increased glutamate escape could be a boost in dendritic NMDAR-dependent spikes (Chalifoux and Carter, 2011), facilitated plasticity at inactive excitatory connections nearby (Tsvetkov et al., 2004), or increased heterosynaptic depression (Vogt and Nicoll, 1999). Intriguingly, our results propose that, by engaging perisynaptic astroglial withdrawal, synaptic potentiation could reduce glutamate uptake near dendritic spines and thus prompt self-excitation of mitral cells in the olfactory bulb (Isaacson, 1999) and boost excitation of interneurons by cerebellar climbing fibers (Coddington et al., 2013). In aged animals, however, astroglial glutamate uptake

reduction could facilitate cognitive decline associated with synaptic loss (Pereira et al., 2014) whereas increased glutamate spillover in the hippocampus could impair aspects of memory related to spatial reference and fear (Tanaka et al., 2013; Tsvetkov et al., 2004). We therefore can conclude that the induction of synaptic plasticity is an important mechanism through which our brain activity can control the extent of glutamate spillover and its consequences for neural circuit function, cognition, and behavior.

AUTHORS CONTRIBUTIONS

D.A.R. and C.H. conceived the study and its research strategies; C.H., L.B., D.M. and M.K.H. carried out patch-clamp recordings, morphometric studies, glutamate uncaging, and glutamate sensor imaging experiments and analyses; A.P., S.H.R.O. and U.V.N. designed and carried out STED experiments; J.P.R. implemented expression of genetic sensors and labels and carried out *in vivo* experiments and analyses; N.I.M., I.K., and M.G.S. designed and carried out 3D EM studies and analyses; I.S.R. and H.J. designed and provided the modified optical glutamate sensor bFLIPE600n; S.R. performed S3 peptide experiments; J.H. designed and carried out dSTORM studies; O.K. carried out 'chemical LTP' experiments; K.Z. performed biophysical modelling tests and dSTORM quantification; S.A. performed some imaging experiments *ex vivo*; T.J. carried out single-axon pairing experiments in slices; O.P.O. and E.A.N. provided expertise and materials pertinent to the AQP4 and pharmacological dissection tests; D.A.R. carried out some data and image analyses and wrote the paper which was subsequently contributed to by all the authors.

ACKNOWLEDGEMENTS

This work was supported by the Wellcome Trust Principal Fellowship, European Research Council Advanced Grant, Medical research Council, Biology and Biotechnology Research Council (all UK), BM1001 Cost Action and FP7 ITN EXTRABRAIN Marie Curie Action (European Commission) (D.A.R.); NRW-Rückkehrerpogramm, Human Frontiers Science Program, UCL Excellence Fellowship, German Research Foundation (DFG) SPP1757 and SFB1089 (C.H.); Human Frontiers Science Program (C.H. and H.J.); EMBO Long-Term Fellowship (L.B.). We thank J. Angibaud for preparation of organotypic cultures, R. Chereau and J. Tonnesen for technical help with the STED microscope. This work was supported by grants from Marie Curie FP7 PIRG08-GA-2010-276995 (A.P.) and Marie Curie Astromodulation (S.R.); Equipe FRM DEQ 201 303 26519, Conseil Régional d'Aquitaine R12056GG, INSERM (S.H.R.O.); ANR SUPERTri, ANR-13-BSV4-0007-01, Université de Bordeaux, labex BRAIN (S.H.R.O., U.V.N.); CNRS, HFSP, ANR CEXC and France-BioImaging ANR-10-INSB-04 (U.V.N.); FP7 MemStick Project No. 201600 (M.G.S.).The authors declare no conflict of interest.

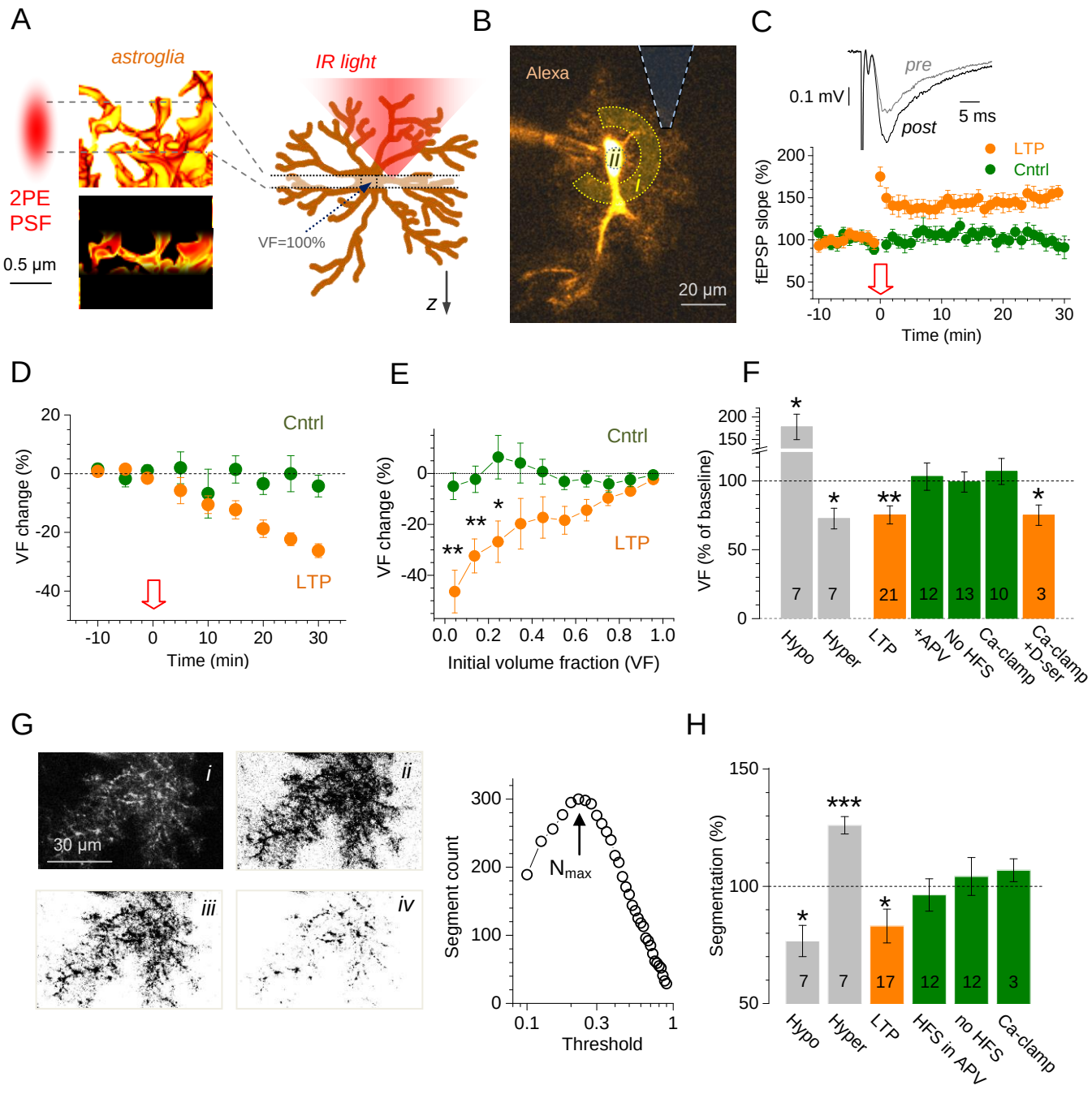

Figure 1. Rapid reduction in astrocyte process presence during LTP at CA3-CA1 synapses.

(A) *Left*: A typical point-spread function (PSF, red) defining a ~1 µm thick two-photon excitation (2PE) plane (*top*, dotted lines) within which a dye-filled astrocyte fragment (yellow, 3D EM reconstruction modified from (Medvedev et al., 2014)) fluoresces (*bottom*). *Right*: diagram showing that intracellular fluorescence within the 2PE plane (dotted lines) scales with astrocyte tissue volume fraction (VF), with VF reaching ~100% when the plane crosses the (5-7 µm wide) soma.

(B) CA1 astrocyte, single 2PE-section image (λ_x^{2p} = 800 nm; Alexa Fluor 594; 50 µM gap-junction blocker carbenoxolone; false colors). Average VF in the focal plane measured as fluorescence intensity within the circular segment (*i*, see Fig. S1A-B for detail; original 16-bit images, background-corrected) relative to that at the soma (*ii)*; dashed lines, the extracellular recording pipette position.

(C) *Traces*, example fEPSPs evoked near a patched astrocyte by stimulating Schaffer collateral, before and ~25 min after LTP induction; *Graph*, time course of normalized fEPSP (mean ± SEM; arrow, LTP induction; average potentiation 25-30 min post-induction: 151.0 ± 6.7% of baseline, $n = 18$).

(D) Astrocyte VF (mean ± SEM) decreases after LTP induction (arrow); average decrease over 25-30 min post-induction: 22.5 ± 2.6% ($n = 13$, $p < 0.001$; orange); VF remains unchanged in control conditions (Cntrl, green; $n = 9$).

(E) LTP-associated astroglial VF reduction (%, mean ± SEM across individual cells) measured pixel-by-pixel (~ 0.3 x 0.3 µm each) across the ROIs shown in B, averaged within individual cells, and plotted against the initial VF (initial VF 0-0.2; Cntrl, $n = 8$ cells; LTP: $n = 13$; * $p < 0.05$, ** $p < 0.01$).

(F) *Grey bars*, VF values relative to baseline (mean ± SEM; sample size n shown) report swelling and shrinkage in hypo-osmotic (220 mOsm/l, Hypo) and hyper-osmotic (420 mOsm/l, Hyper) solutions. *Green and orange bars*: relative VF change 25-30 min after LTP induction protocol in control conditions (LTP, -25 ± 7%), in 50 µM APV (+APV, 3.1 ± 9.9%), with no HFS (-0.8 ± 7.3%), under intra-astrocyte Ca^{2+} clamp (Ca-clamp, 6.8 ± 9.5%) (Henneberger et al., 2010), under Ca^{2+} clamp with 10 µM D-serine added (Ca-clamp+ D-ser, -24 ± 7%); **$p < 0.01$; *$p < 0.05$.

(G) Segmentation measure binarizes the original fluorescent image (image panels: *i*, , astroglial fragment, single 2PE section) and calculates the number of individual binary particles throughout all threshold values (*ii-iv*) to establish the maximum number N_{max} of discernible fragments (plot), independently of brightness (also Fig. S1D-F).

(H) Segmentation (relative to baseline, mean ± SEM; sample size n shown) in tests depicted in F (same notations apply). Note that both VF (F) and Segmentation (H) decrease during LTP while showing opposite changes during osmotic tests (F, H), indicating mutual independence for the two measures (also Fig. S1G).

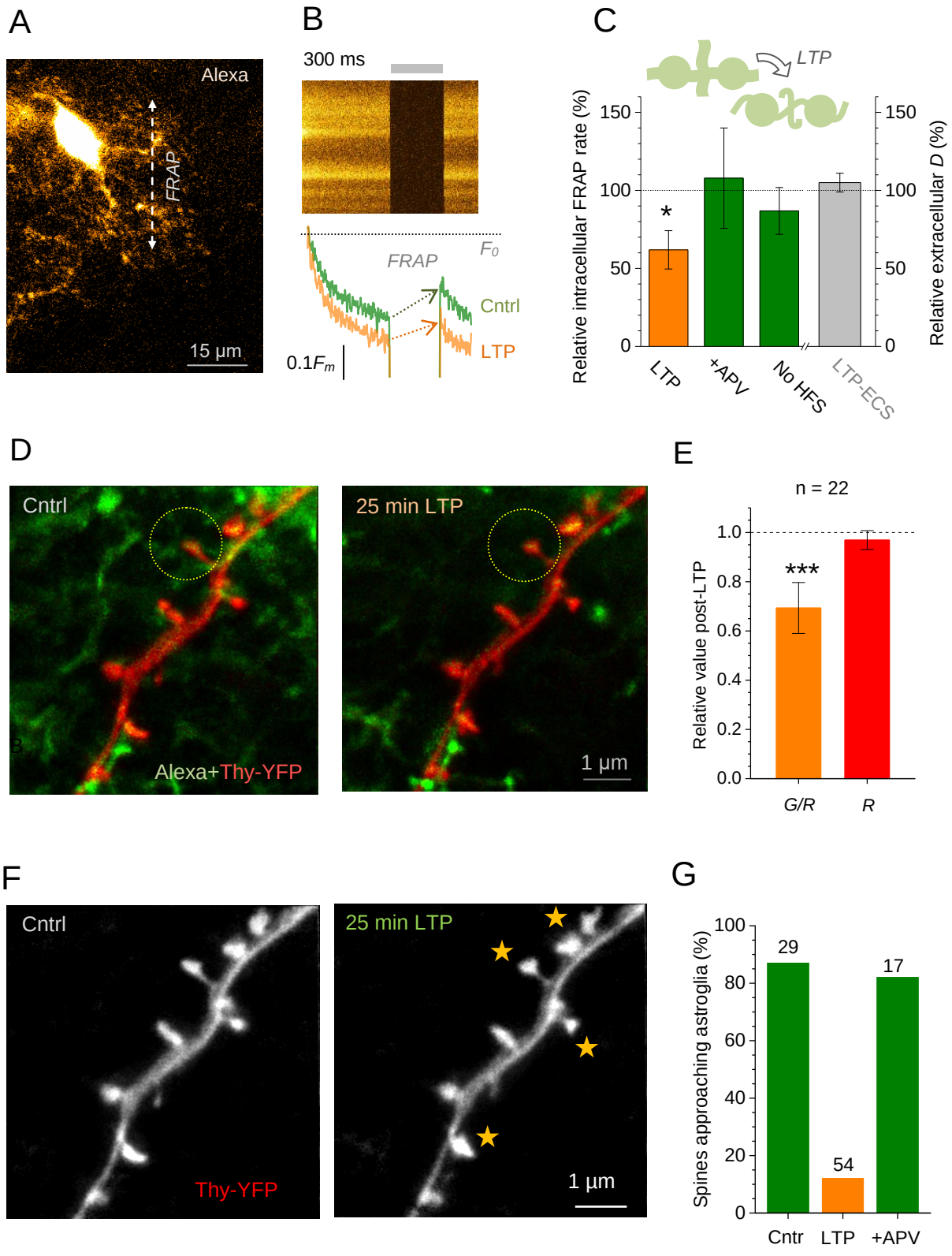

Figure 2. FRAP and live STED microscopy document sub-diffraction changes in perisynaptic astroglia after LTP induction.

(A) Evaluating diffusion connectivity among optically unresolvable astrocyte processes using intracellular dye photobleaching (Method Details). Example of linescan positioning in a single 2PE plane of a CA1 astrocyte filled whole-cell with Alexa Fluor 594 (~80 μm depth in an acute slice).

(B) *Top*: A trace generated by linescan in A (baseline conditions; grey segment, shutter closed). *Bottom*: The corresponding average fluorescence intensity time course before and ~20 min after LTP induction, as indicated; F_0, initial fluorescence intensity; arrows (FRAP) indicate the period and the degree of fluorescence recovery during the shutter-closed period (full recovery normally took 39-40 s).

(C) Summary of tests shown in A-B; inset diagram, LTP induction reducing thinner parts of astroglial processes hence lowering diffusion exchange; plot, FRAP rate relative to baseline (mean ± SEM, left ordinate): LTP, change -38.1 ± 12.3% (n = 11; $p < 0.05$); in the presence of APV, change 7.9 ± 32.2% (n = 7); without HFS stimuli, change -13.1 ± 15.0% (n = 8). *Grey bar* (right ordinate): extracellular diffusion coefficient change post-LTP (LTP-ECS; 107 ± 7 % of baseline, n = 8; also Fig. S2A-C).

(D) Characteristic STED images of CA1 pyramidal cell dendritic spines (red, Thy1-YFP) and nearby astroglia (green; 600 μM Alexa Fluor 488 whole-cell loading) before and ~25 min after LTP induction, as indicated (Method Details); dotted circles, 1.5 μm-wide regions of interests (ROIs) centered at the spine head.

(E) LTP induction reduces the green/red (astroglia/neuron) average intensity ratio (orange; mean ± SEM for pixel counts) within the spine-associated ROIs (by 31 ± 10%, n = 22, ***$p < 0.001$; whole-cell dialysis rules out long-term photobleaching), without affecting neuronal labelling (red pixel counts; change - 3.1 ± 3.8%, n = 22).

(F) Same fragments as in D but under optimized STED settings in a Thy-YFP channel. Stars, visible alterations in spine head geometry after LTP induction (see Fig S2D-E for further detail).

(G) Average fraction of dendritic spines adjacent to astroglial processes in baseline conditions (Cntr), 20-25 min after LTP induction (LTP), and under the induction protocol in the presence of 50 μM APV.

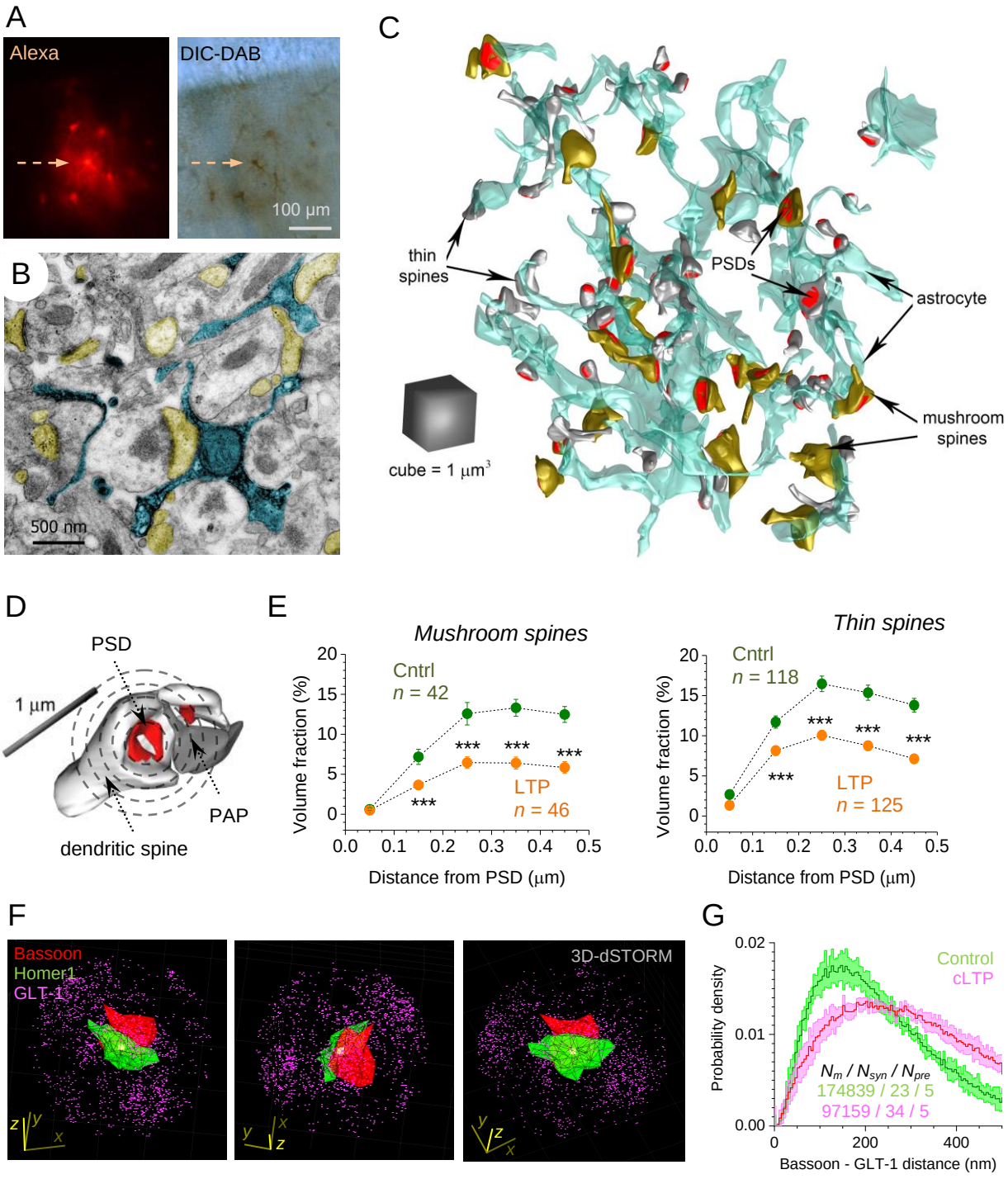

Figure 3. 3D correlational EM and super-resolution dSTORM report reduced PAP presence after LTP induction.

(A) *Top*: recorded astrocyte (arrow) loaded with biocytin (neighboring astroglia stained through gap junctions), shown in fluorescence (*left*) and DIC channel after DAB conversion (*right*).

(B) Electron micrograph showing thin processes of the astrocyte in A filled with precipitate (light blue) and dendritic spine sections (yellow) containing PSDs (dense lines); astrocyte 3D tracing was verified under visual control (Method Details).

(C) Fragment of a recorded astrocyte (as in A, cyan) reconstructed in 3D from ~60 nm serial sections, including adjacent thin (white) and mushroom (yellow) dendritic spines containing PSDs (red; Fig. S3).

(D) An integrative (volumetric) measure of synaptic astroglial coverage: VF occupied by astroglia is calculated within 100 nm-wide concentric 3D shells (dotted circles, not to scale) centered at the PSD (red).

(E) The astroglia VF distribution around PSDs (mean ± SEM), for thin and mushroom dendritic spines adjacent to the recorded astrocyte (as in D), in baseline conditions and ~30 min after LTP induction, as indicated; sample sizes are shown; *** $p < 0.001$.

(F)) 3D three-color dSTORM, one-synapse example (*s.radiatum*): molecular patterns for presynaptic bassoon (CF-568, red), postsynaptic Homer 1 (Atto-488, green), and glutamate transporter GLT-1 (Alexa-647, magenta); three viewing angles shown, with bassoon and Homer1 patterns depicted as solid clusters, for clarity; *x-y-z* axes, scale bars 500 nm; photoswitching buffer, 100 mM cysteamine and oxygen scavengers (glucose oxidase and catalase).

(G) Average distribution (probability density, mean ± SEM) of the nearest-neighbour distances (<500 nm) between GLT-1 and synaptic Bassoon molecules in control and potentiated tissue (~30 min after 'chemical' LTP induction, see Method Details); a summary for a total of N_m inter-molecular distances at N_{syn} synapses from N_{pre} individual preparations (slices), as indicated; SEM calculated for the variance among $N_{pre} = 5$ (conservative estimate); the SEM band corresponds to ~95% confidence limit to reject the null-hypothesis, independently bin-by-bin.

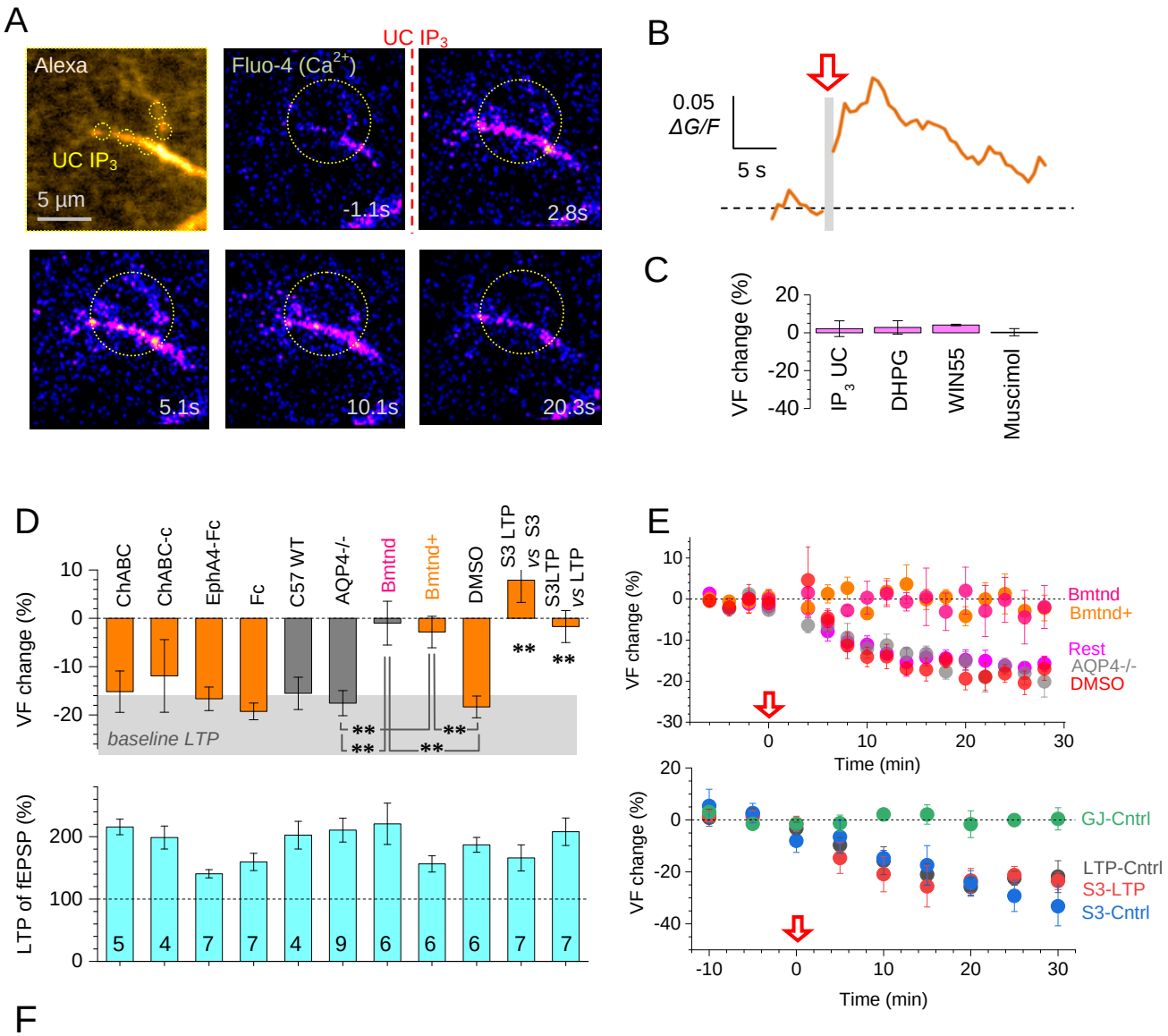

Figure 4. LTP-triggered PAP withdrawal does not depend on major astroglial Ca^{2+} cascades, ephrins, or aquaporin but relies on NKCC1 and cofilin.

(A) *Top left panel*; an astrocyte fragment (5 µm deep z-stack) depicting sites of intracellular IP3 spot-uncaging (dotted circles; Alexa Fluor 594 channel, λ_x^{2P} = 840 nm). *Other panels:* Frame scans depicting astroglial Ca^{2+} rises (Fluo-4 channel; false colors) evoked by IP3 spot-uncaging (IC IP_3, red dotted line, onset at time zero; 5 ms pulses 200 ms apart, five cycles over all the spots, λ_u^{2P} = 720 nm), as shown; time stamps indicated; dotted circle, ROI for Ca^{2+} monitoring.

(B) Time course of intracellular astroglial Ca^{2+} signal ($\Delta F/G$) in the ROI shown in A; one-cell example; red arrow and shaded area, IP_3 uncaging.

(C) Summary: experiments shown in A-B, and activation of other major astroglial Ca^{2+} -signaling cascades had no effect on local astroglial VF. Ordinate, VF (relative to baseline, mean ± SEM) 25 min after: spot-uncaging of intracellular IP_3 (change 2.2 ± 4.2%, n = 7), the application of group I mGluR agonist DHPG (300 µM, pressure-puff pipette application, 2.8 ± 3.6%, n = 6), of CB1 receptor agonist WIN55 (1 µM, 4.1 ± 0.4%, n = 3), and of GABA receptor agonist muscimol (20 µM, -0.3 ± 1.9%, n = 6).

(D) *A*stroglial VF changes relative to baseline (*top*, mean ± SEM, sample size shown) 25 min post LTP induction, and the corresponding LTP expression level (*bottom*) in a battery of tests: in the presence of 0.5-0.7 U/ml Chondroitinase ABC (ChABC, -15 ± 4%), control ChABC-c (-12 ± 8%), 10 µg/ml EphA4-Fc (-17 ± 2%), 10 µg/ml Fc control (-19 ± 2%), wild-type C57BI6 mice (-16 ± 3%), $AQP4^{-/-}$ knockout mice (-18 ± 3%), 20 µM intracellular bumetanide (Bmtnd, -0.5 ± 4.5%), 50 µM intracellular bumetanide + 100 µM extracellular TGN-020 (Bmtnd+, -2.8 ± 3.2%), DMSO control 0.2% external + 0.05% internal (-18 ± 2%); VF post-LTP under S3 relative to VF under S3 only (S3 LTP vs S3, 7.9 ± 4.6%); VF post-LTP under S3 relative to VF post-LTP only (-1.7 ± 3.3%), as indicated; dark pink bars, data obtained in mice; grey shadow area, mean ± SEM interval for the VF change during LTP induction in control conditions (as in Fig. S4D); ** $p < 0.01$ (t-test or Mann-Whitney independent sample tests).

(E) *Top*, time course of relative VF (mean ± SEM) during LTP induction (HFS, arrow) shown for key experiments described in D, as indicated, and the summary data for the rest of experiments (Rest); *bottom*, time course of astroglial VF (mean ± SEM) in S3 peptide (occlusion) experiments: GJ-Ctrl, gap-junction connected astroglia (no HFS); LTP-Cntrl, LTP induction without S3; S3-LTP, LTP induction with S3 inside astroglia; S3-Cntrl, S3 inside astroglia without LTP induction; arrow, LTP induction onset where applies; sample size and stats as in D.

(F) Candidate cellular mechanisms involved in the LTP-driven PAP withdrawal (grey arrows). Red stars, essential players: LTP induction through activation of postsynaptic NMDA receptors rapidly changes ion homeostasis inside and near the synaptic cleft, thus engaging astroglial NKCC1 which trigger morphological changes in PAPs by activating the actin-regulating protein cofilin-1. See Discussion for detail.

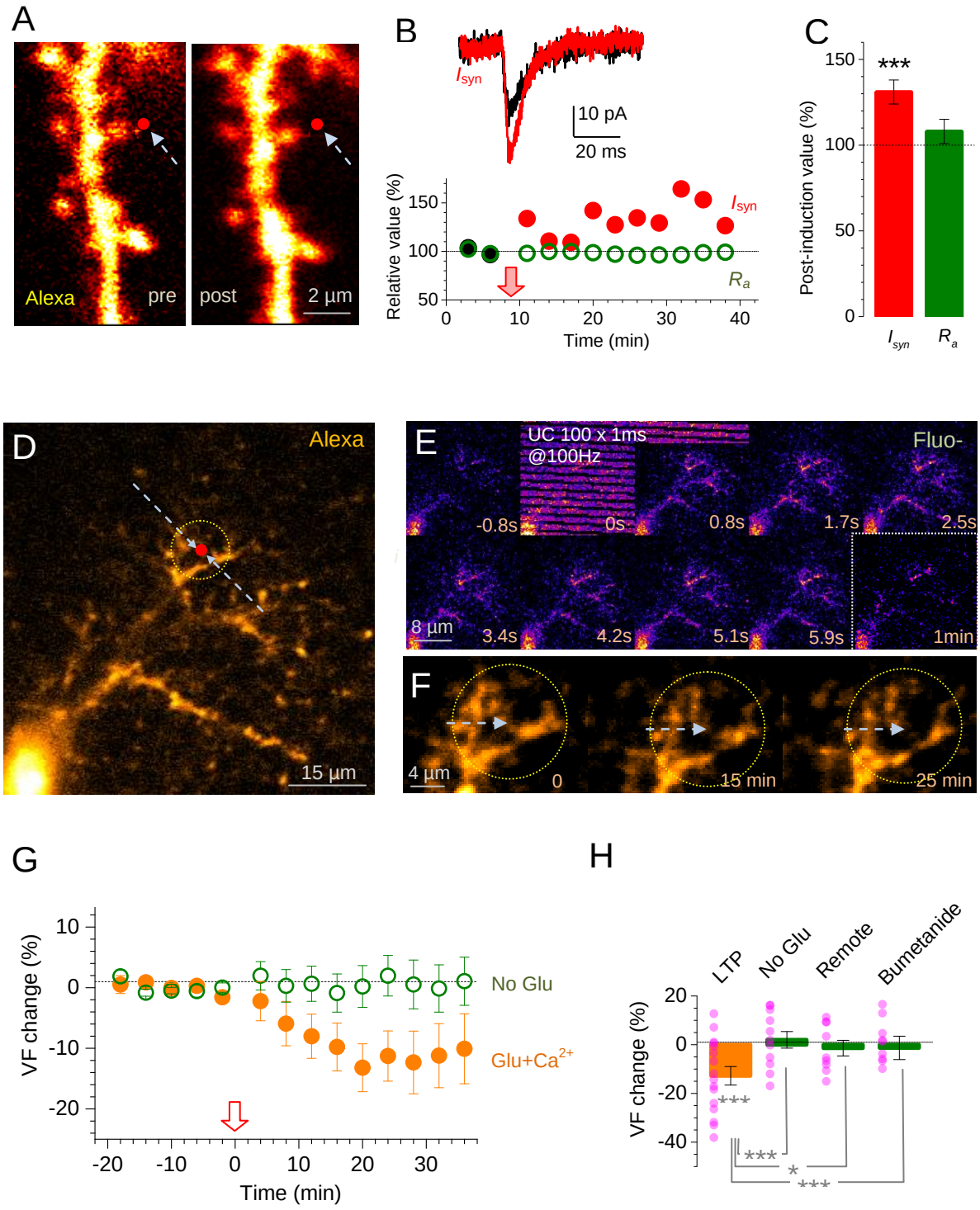

Figure 5. LTP induction at individual CA3-CA1 synapses reduces local astroglial presence.

(A) Dendritic fragment of a CA1 pyramidal cell showing spot-uncaging position (arrow, red dot) before (pre) and 20 min after LTP induction uncaging protocol (post).

(B) *Traces*: inset, EPSCs (I_{syn}, voltage-clamp) during baseline (black) and ~30 min after LTP induction (red) in tests shown in A (Method Details; see Fig. S4A-B for postsynaptic Ca^{2+} recordings). *Graph*:

one-cell example, time course of uncaging-evoked single-spine EPSC amplitude (I_{syn}; black, baseline; red, post-induction; arrow, LTP induction onset) and cell access resistance (R_a, green) in the same experiment.

(C) Statistical summary of experiments depicted in A-B (mean ± SEM; n = 7, ***p < 0.005); notations as in B.

(D) Example of an astrocyte fragment (Alexa Fluor 594, single 2PE plane) showing spot-uncaging position (arrows, red dot) and ROI for local monitoring of astroglial VF.

(E) Frame scans depicting astroglial [Ca^{2+}] rises (Fluo-4, λ_x^{2P} = 840 nm) evoked by the spot-uncaging LTP induction protocol (UC; 100 x 1 ms pulses at 100 Hz, three times every 60 s) in the cell shown in D (zoomed out); bleed-through time stamp for uncaging (λ_u^{2P} = 720 nm) is seen in frame 0-0.8s.

(F) Expanded area *i* (shown in D) immediately upon, at 15 min and 25 min after the spot-uncaging LTP induction (arrow; ~9 µm high *z*-stack average); retraction of some astroglia processes could be seen at 15-25 min post-stimulus.

(G) Time course of average normalized VF (mean ± SEM) in experiments depicted in D-E (orange, Glu+Ca^{2+}, n = 11), and in the control group with no MNI-glutamate (No Glu, n = 11).

(H) Statistical summary for experiments shown in G**:** average VF change after the glutamate uncaging protocol with a detectable Ca^{2+} response (Glu+Ca^{2+}, -12 ± 5%, *P < 0.04, n = 11), with no MNI-glutamate present (no Glu, 2.0 ± 3.4%, n = 6), in remote ROI (>3 µm away from the uncaging spot; Remote, -1.4 ±3.2%, n = 11), and in the presence of 20 µM NKCC1 blocker bumetanide inside the cell (Bumetanide, -1.3 ± 4.8%, n = 9); * p < 0.05; *** p < 0.005.

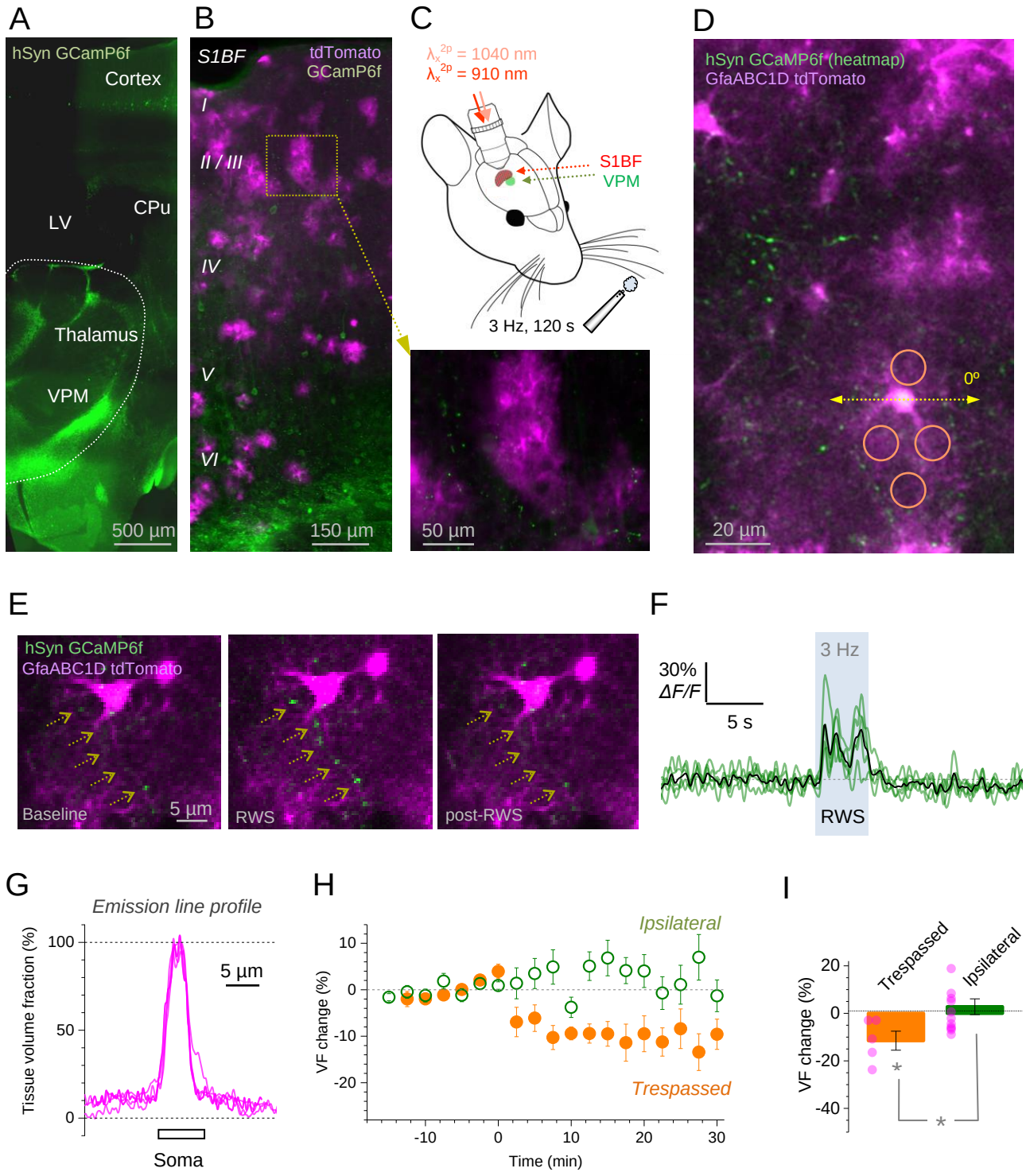

Figure 6. Whisker-stimulation LTP protocol in the barrel cortex *in vivo* triggers volume reduction in astroglia trespassed by stimulated axons.

(A) Low-resolution brain slice fluorescence image (coronal section) illustrating the expression of the Ca^{2+} indicator GCaMP6f three weeks after its transfection (AAV9) into the mouse ventral posteromedial nucleus (VPM); LV, lateral ventricle; CPu caudate putamen.

(B) Composite fluorescence image of the barrel cortex area of interest (coronal section), with astroglia expressing GfaABC1D tdTomato (magenta; transfection with AAV5) and neuronal structures expressing GCaMPf6 (green); dotted rectangle and magnified inset (yellow arrow) illustrate two astrocytes with numerous axonal bouton projections occurring nearby (green); excitation at λ_x^{2p} = 1040 nm (tdTomato) and λ_x^{2p} = 910 nm (GCamPf6).

(C) Experiment diagram: 2PE imaging of the barrel cortex (S1BF) through a cranial window, with two femtosecond lasers as indicated. The LTP induction protocol uses rhythmical whisker stimulation (RWS, 5 Hz air puff stimuli for 120 s) on the contralateral side.

(D) Typical barrel cortex view (S1BF) through the cranial window (excitation at λ_x^{2p} = 1040 nm and λ_x^{2p} = 910 nm) depicting the heat map of axons firing in response to whisker stimulation (GCaMPf6, green) and local astroglia expressing tdTomato (magenta). Orange circles: volume fraction ROIs in an astrocyte 'trespassed' by multiple whisker-responding axons (green). Dashed arrow (yellow), line readout of astroglia emission intensity profile at (line sampled at 0º); see E below.

(E) Example of individual axonal boutons in S1BF (dashed arrows) responding to a short burst of RWS (3 Hz for 5s) with Ca^{2+} elevations (GCaMP6f, green channel) while trespassing local astroglia (tdTomato, magenta), as indicated.

(F) Time course of axonal Ca^{2+} signal from five individual axonal boutons (green lines) shown in (D); black line, average.

(G) Example of the astroglial VF profile along the line shown in (D) by yellow arrow (0º), and also at 45º, 90º, and 135º (tdTomato channel, normalized against somatic fluorescence). The profile is similar that in whole-cell dialyzed astroglia (Fig. S1B).

(H) Average time course (mean ± SEM) of VF change, before and after the RWS LTP induction protocol, in barrel cortex astrocytes 'trespassed' by the firing axons (orange circles, n = 5 cells from three animals) and in control astroglia where the RWS was performed on the ipsilateral whiskers (n = 12 cells from four animals).

(I) Statistical summary of experiments shown in (G) for the VF change between 15-30 min after the LTP induction protocol; bars, mean ± SEM; dots, data from individual cells; * $p < 0.04$.

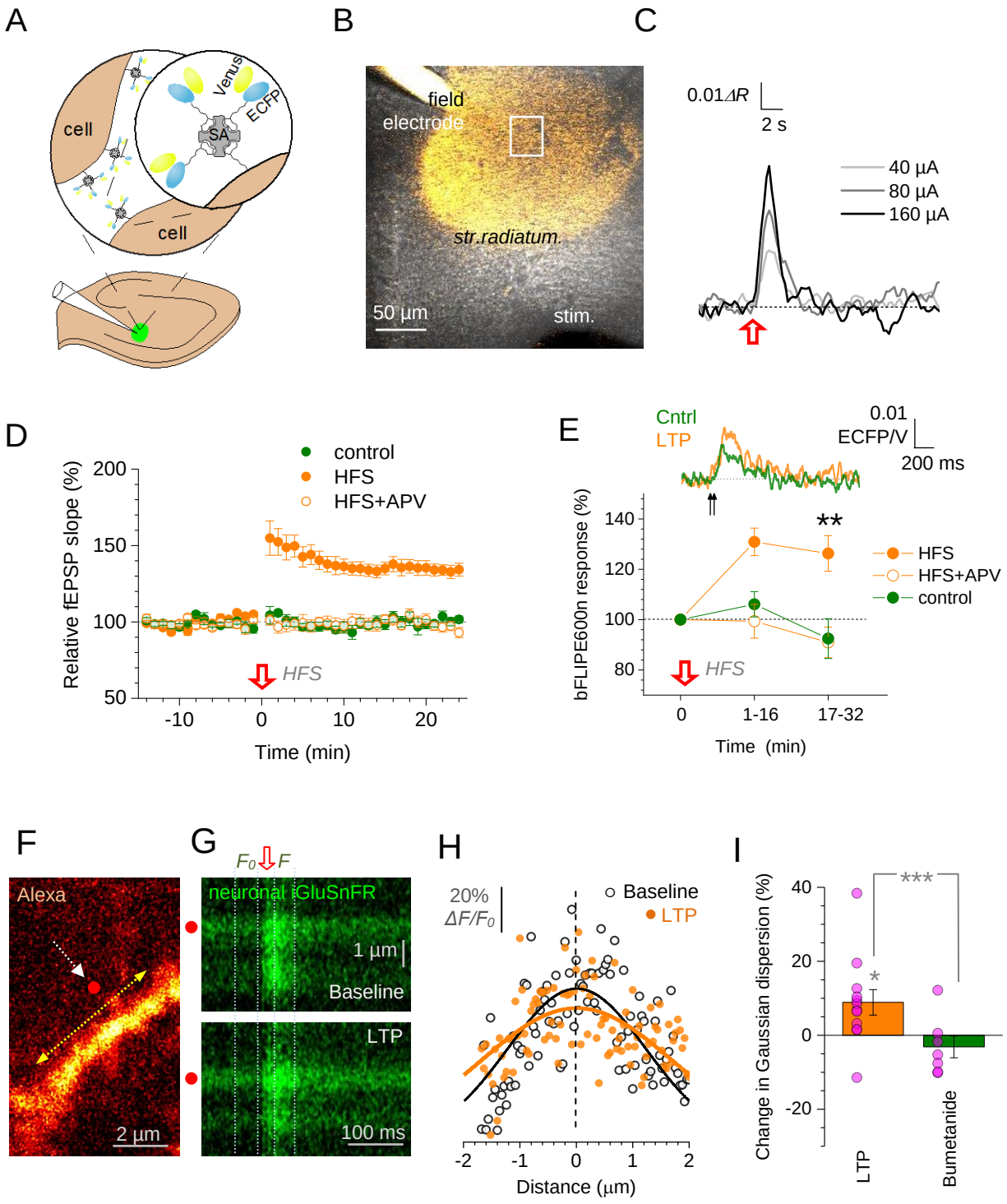

Figure 7. LTP induction expands glutamate transients in the extrasynaptic space.

(A) Schematic illustrating extracellular immobilization of the high-affinity glutamate sensor bFLIPE600n (Venus and ECFP fluorophore attachments indicated) in the extracellular space via biotinylation with a commercially available agent and an attachment to streptavidin (SA, Fig. S5B-C; Method Details) (Okubo *et al.*, 2010). The sensor is injected into the CA1 *s. radiatum* in acute slices

using a pressurized patch pipette (indicated). Glutamate binding alters FRET between Venus and ECFP thus reporting glutamate concentration.

(B) Experimental arrangement: fEPSPs evoked by electrical stimulation of Schaffer collaterals (stim) were monitored using the sensor-injection pipette electrode (field).

(C) Example of extrasynaptic glutamate transients reported by bFLIPE600n (ΔR, ECFP/Venus intensity ratio) in response to Schaffer collateral HFS (100 Hz for 1 s, red arrow; 10 µM NBQX, 50 µM D-APV in the bath) in *s. radiatum*. Traces normalized to baseline; input-output calibration summaries shown in Fig. S5B-C.

(D) The fEPSP slope (mean ± SEM) relative to baseline at time zero in control experiments (green, n = 8 slices) and during LTP induction (orange), with and without 50 µM D-APV in the bath solution experiment (n = 7 and n = 14, empty and filled circles, respectively); ** $p < 0.01$.

(E) Traces, examples of optical bFLIPE600n responses induced by a Schaffer collateral stimulus (two pulses 50 ms apart) in baseline conditions (green) and ~25 min after induction of LTP (orange), as indicated. Plot, summary of experiments shown in (D) (one-way ANOVA and Fisher post-hoc test at 17-32 min time point control vs HFS p = 0.0019, HFS vs HFS in D-APV p = 0.00396; other notations as in D).

(F) Dendritic fragment of a CA1 pyramidal cell (2PE, Alexa Fluor 594 channel); red dot, glutamate uncaging spot; dashed arrow, line scan positioning for iGluSnFR fluorescence monitoring.

(G) Line scans (position as in F; 2PE, iGluSnFR channel) illustrating extracellular glutamate-sensitive fluorescence transients in response to 1 ms glutamate spot-uncaging (arrow, timing; red dot, position); shown in baseline (*top*) and 20-25 min after applying the spot-uncaging LTP-induction protocol (*bottom*), as indicated; dotted lines, sampling regions for the baseline (F_0) and evoked (F) fluorescence profiles: the uncaging induced signal profile was calculated as $\Delta F = F - F_0$ (Methods details).

(H) Example of spatial glutamate-sensitive fluorescence profiles (dots, individual pixel values) evoked by a 1 ms glutamate uncaging pulse, before (Baseline) and 20-25 min after LTP induction, as indicated, in experiments illustrated in F-G; zero abscissa, the uncaging spot position; black and orange solid lines, best-fit Gaussian approximation of the glutamate signal spread.

(I) Summary of experiments shown in (F-H); dots, relative change in the best-fit iGluSnFR signal dispersion (glutamate spread) parameter (Gaussian standard deviation) in individual experiments; columns, mean ± SEM. LTP, 25 min after LTP induction versus baseline (9.0 ± 3.4%; n = 12; *, p=0.027); Bumetanide, similar experiments with 20 µM bumetanide inside astroglia (-2.5 ± 3.2%; n = 7; difference with LTP at ***$p < 0.005$).

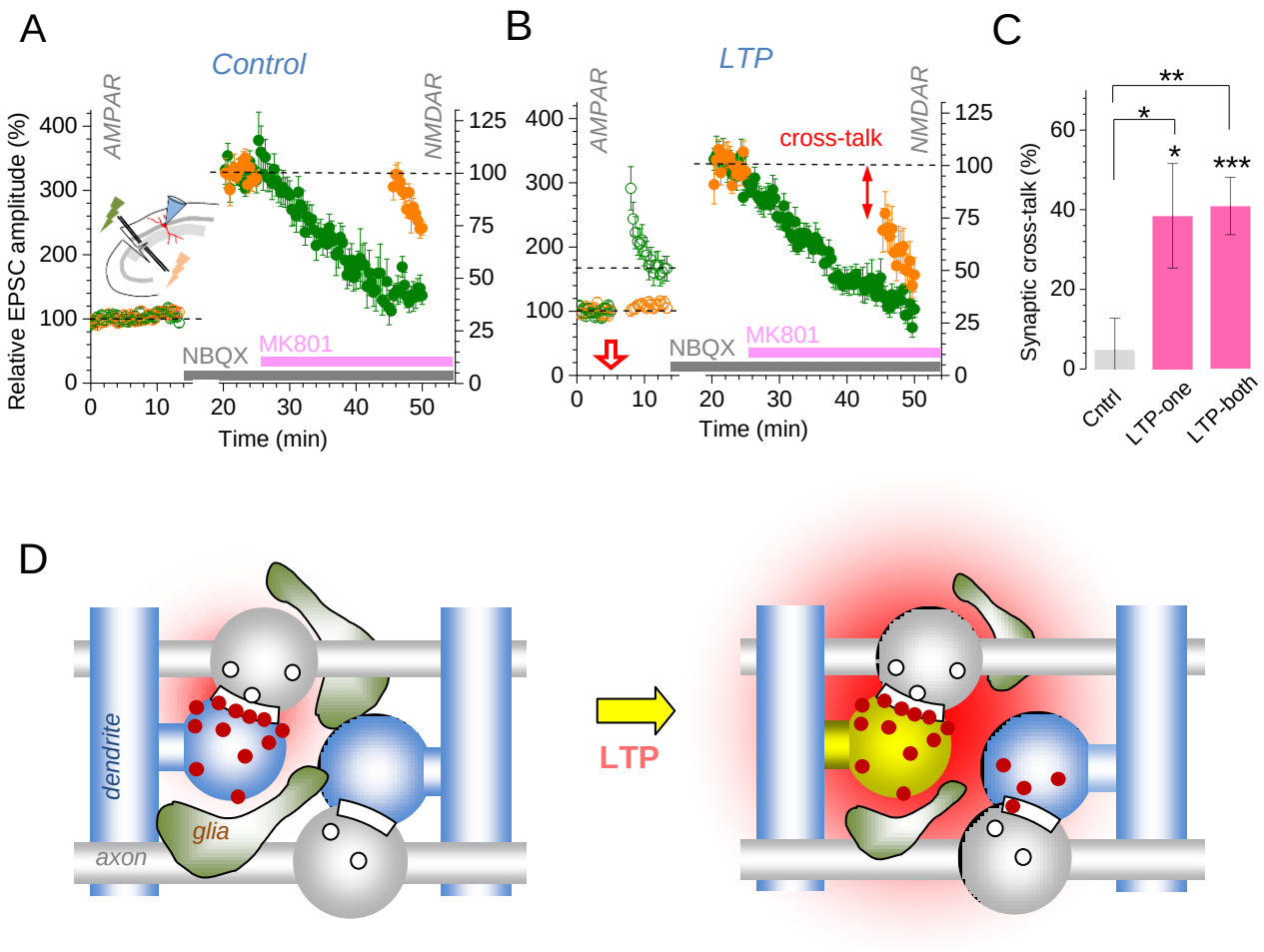

Figure 8. LTP induction enhances glutamate escape from synapses boosting NMDAR-mediated inter-synaptic cross-talk.

(A) *Inset diagram*, a previously established test for NMDAR-mediated cross-talk between two independent CA3-CA1 afferent pathways (green and orange lightning) (Method detail; Fig. S6D). *Plot*, time course of EPSC amplitude (mean ± SEM, n = 13) evoked by single stimuli applied alternately to the two pathways (green and orange; inter-stimulus interval 20 s). First, AMPAR EPSCs are recorded in both pathways (V_m = -70 mV; left ordinate) for ~12-15 min, then NMDAR EPSCs (10 µM NBQX, V_m = -20 mV; right ordinate) for ~5 min, then MK801 is added while the progressively blocked NMDAR EPSCs are recorded in one (control, green) pathway while the other is kept silent (orange, no stimuli). Resuming stimulation in the silent (orange) pathway shows little change in the NMDAR EPSC amplitude compared to baseline (dotted line).

(B) Experiment as in (A) but with LTP induced in one pathway (hollow red arrow; n = 7). The reduced amplitude of NMDAR EPSCs in the silent (orange) pathway upon resumed stimulation (double-headed red arrow, cross-talk) indicated NMDAR activation by glutamate released from the other (active) pathway.

(C) Summary of experiments shown in (A-B). The amount of inter-pathway cross-talk (percentage of NMDARs on one pathway activated by glutamate released from the other pathway; mean ± SEM) is shown, in control conditions (Cntrl, n = 13), with LTP induced either in one (LTP-one, n = 10) or both (LTP-both, n = 11; Fig. S8C-D) afferent pathways, prior to NMDAR EPSC recordings; * $p < 0.05$, ** $p < 0.01$, *** $p < 0.001$.

(D) The proposed scenario of architectural changes in the synaptic astroglial microenvironment after LTP induction. In baseline conditions (*left*), PAPs restrict glutamate action to the synaptic cleft and some adjacent high-affinity receptors such as NMDARs (red shade; red dots). Following LTP induction (*right*), some PAPs withdraw, allowing activation of a wider pool of NMDARs outside activated synapses including neighboring synapses.

REFERENCES

Adamsky, A., Kol, A., Kreisel, T., Doron, A., Ozeri-Engelhard, N., Melcer, T., Refaeli, R., Horn, H., Regev, L., Groysman, M., *et al.* (2018). Astrocytic Activation Generates De Novo Neuronal Potentiation and Memory Enhancement. Cell *174*, 59-71 e14.

Aizawa, H., Wakatsuki, S., Ishii, A., Moriyama, K., Sasaki, Y., Ohashi, K., Sekine-Aizawa, Y., Sehara-Fujisawa, A., Mizuno, K., Goshima, Y., *et al.* (2001). Phosphorylation of cofilin by LIM-kinase is necessary for semaphorin 3A-induced growth cone collapse. Nat Neurosci *4*, 367-373.

Anders, S., Minge, D., Griemsmann, S., Herde, M.K., Steinhauser, C., and Henneberger, C. (2014). Spatial properties of astrocyte gap junction coupling in the rat hippocampus. Philos Trans R Soc Lond B Biol Sci *369*, 20130600.

Arnth-Jensen, N., Jabaudon, D., and Scanziani, M. (2002). Cooperation between independent hippocampal synapses is controlled by glutamate uptake. Nature Neurosci *5*, 325-331.

Bernardinelli, Y., Randall, J., Janett, E., Nikonenko, I., Konig, S., Jones, E.V., Flores, C.E., Murai, K.K., Bochet, C.G., Holtmaat, A., *et al.* (2014). Activity-dependent structural plasticity of perisynaptic astrocytic domains promotes excitatory synapse stability. Curr Biol *24*, 1679-1688.

Bliss, T.V.P., Douglas, R.M., Errington, M.L., and Lynch, M.A. (1986). Correlation between Long-Term Potentiation and Release of Endogenous Amino-Acids from Dentate Gyrus of Anesthetized Rats. J Physiol *377*, 391-408.

Bloodgood, B.L., and Sabatini, B.L. (2005). Neuronal activity regulates diffusion across the neck of dendritic spines. Science *310*, 866-869.

Bravo-Cordero, J.J., Magalhaes, M.A., Eddy, R.J., Hodgson, L., and Condeelis, J. (2013). Functions of cofilin in cell locomotion and invasion. Nat Rev Mol Cell Biol *14*, 405-415.

Bushong, E.A., Martone, M.E., Jones, Y.Z., and Ellisman, M.H. (2002). Protoplasmic astrocytes in CA1 stratum radiatum occupy separate anatomical domains. J Neurosci *22*, 183-192.

Carter, A.G., and Regehr, W.G. (2000). Prolonged synaptic currents and glutamate spillover at the parallel fiber to stellate cell synapse. J Neurosci *20*, 4423-4434.

Chalifoux, J.R., and Carter, A.G. (2011). Glutamate Spillover Promotes the Generation of NMDA Spikes. J Neurosci *31*, 16435-16446.

Coddington, L.T., Rudolph, S., Vande Lune, P., Overstreet-Wadiche, L., and Wadiche, J.I. (2013). Spillover-Mediated Feedforward Inhibition Functionally Segregates Interneuron Activity. Neuron *78*, 1050-1062.

Danbolt, N.C. (2001). Glutamate uptake. Progr Neurobiol *65*, 1-105.

Diamond, J.S. (2002). A broad view of glutamate spillover. Nat Neurosci *5*, 291-292.

Diamond, J.S., Bergles, D.E., and Jahr, C.E. (1998). Glutamate release monitored with astrocyte transporter currents during LTP. Neuron *21*, 425-433.

Dityatev, A., and Rusakov, D.A. (2011). Molecular signals of plasticity at the tetrapartite synapse. Curr Opin Neurobiol *21*, 353-359.

Dityatev, A., and Schachner, M. (2003). Extracellular matrix molecules and synaptic plasticity. Nat Rev Neurosci *4*, 456-468.

Endesfelder, U., and Heilemann, M. (2015). Direct stochastic optical reconstruction microscopy (dSTORM). Methods Mol Biol *1251*, 263-276.

Epsztein, J., Lee, A.K., Chorev, E., and Brecht, M. (2010). Impact of spikelets on hippocampal CA1 pyramidal cell activity during spatial exploration. Science *327*, 474-477.

Errington, M.L., Galley, P.T., and Bliss, T.V.P. (2003). Long-term potentiation in the dentate gyrus of the anaesthetized rat is accompanied by an increase in extracellular glutamate: real-time measurements using a novel dialysis electrode. Phil Trans Roy Soc ser B *358*, 675-687.

Ethell, I.M., and Pasquale, E.B. (2005). Molecular mechanisms of dendritic spine development and remodeling. Prog Neurobiol *75*, 161-205.

Fanelli, A., Titapiccolo, J.I., Esposti, F., Ripamonti, M., Malgaroli, A., and Signorini, M.G. (2011). Novel image processing methods for the analysis of calcium dynamics in glial cells. Ieee Transactions on Biomedical Engineering *58*, 2640-2647.

Filosa, A., Paixao, S., Honsek, S.D., Carmona, M.A., Becker, L., Feddersen, B., Gaitanos, L., Rudhard, Y., Schoepfer, R., Klopstock, T., *et al.* (2009). Neuron-glia communication via EphA4/ephrin-A3 modulates LTP through glial glutamate transport. Nat Neurosci *12*, 1285-1292.

Florence, C.M., Baillie, L.D., and Mulligan, S.J. (2012). Dynamic Volume Changes in Astrocytes Are an Intrinsic Phenomenon Mediated by Bicarbonate Ion Flux. PLoS One *7*.

Frick, A., Magee, J., and Johnston, D. (2004). LTP is accompanied by an enhanced local excitability of pyramidal neuron dendrites. Nat Neurosci *7*, 126-135.

Gambino, F., Pages, S., Kehayas, V., Baptista, D., Tatti, R., Carleton, A., and Holtmaat, A. (2014). Sensory-evoked LTP driven by dendritic plateau potentials in vivo. Nature *515*, 116-119.

Garzon-Muvdi, T., Schiapparelli, P., ap Rhys, C., Guerrero-Cazares, H., Smith, C., Kim, D.H., Kone, L., Farber, H., Lee, D.Y., An, S.S., *et al.* (2012). Regulation of brain tumor dispersal by NKCC1 through a novel role in focal adhesion regulation. PLoS Biol *10*, e1001320.

Grosche, J., Matyash, V., Moller, T., Verkhratsky, A., Reichenbach, A., and Kettenmann, H. (1999). Microdomains for neuron-glia interaction: parallel fiber signaling to Bergmann glial cells. Nat Neurosci *2*, 139-143.

Haas, B.R., and Sontheimer, H. (2010). Inhibition of the Sodium-Potassium-Chloride Cotransporter Isoform-1 reduces glioma invasion. Cancer Res *70*, 5597-5606.

Habela, C.W., Ernest, N.J., Swindall, A.F., and Sontheimer, H. (2009). Chloride accumulation drives volume dynamics underlying cell proliferation and migration. J Neurophysiol *101*, 750-757.

Haber, M., Zhou, L., and Murai, K.K. (2006). Cooperative astrocyte and dendritic spine dynamics at hippocampal excitatory synapses. J Neurosci *26*, 8881-8891.

Hama, H., Kurokawa, H., Kawano, H., Ando, R., Shimogori, T., Noda, H., Fukami, K., Sakaue-Sawano, A., and Miyawaki, A. (2011). Scale: a chemical approach for fluorescence imaging and reconstruction of transparent mouse brain. Nat Neurosci *14*, 1481-1488.

Harris, K.M., Jensen, F.E., and Tsao, B. (1992). Three-dimensional structure of dendritic spines and synapses in rat hippocampus (CA1) at postnatal day 15 and adult ages: implications for the maturation of synaptic physiology and long-term potentiation. J Neurosci *12*, 2685-2705.

Harvey, C.D., and Svoboda, K. (2007). Locally dynamic synaptic learning rules in pyramidal neuron dendrites. Nature *450*, 1195-U1193.

Heller, J.P., Michaluk, P., Sugao, K., and Rusakov, D.A. (2017). Probing nano-organization of astroglia with multi-color super-resolution microscopy. J Neurosci Res *95*, 2159-2171.

Heller, J.P., and Rusakov, D.A. (2015). Morphological plasticity of astroglia: Understanding synaptic microenvironment. Glia *63*, 2133-2151.

Henneberger, C., Papouin, T., Oliet, S.H., and Rusakov, D.A. (2010). Long-term potentiation depends on release of D-serine from astrocytes. Nature *463*, 232-236.

Henneberger, C., and Rusakov, D.A. (2012). Monitoring local synaptic activity with astrocytic patch pipettes. Nature Protocols *7*, 2171-2179.

Hires, S.A., Zhu, Y., and Tsien, R.Y. (2008). Optical measurement of synaptic glutamate spillover and reuptake by linker optimized glutamate-sensitive fluorescent reporters. Proc Natl Acad Sci U S A *105*, 4411-4416.

Hirrlinger, J., Hulsmann, S., and Kirchhoff, F. (2004). Astroglial processes show spontaneous motility at active synaptic terminals in situ. Eur J Neurosci *20*, 2235-2239.

Hoffmann, E.K., Lambert, I.H., and Pedersen, S.F. (2009). Physiology of Cell Volume Regulation in Vertebrates. Physiol Rev *89*, 193-277.

Igarashi, H., Huber, V.J., Tsujita, M., and Nakada, T. (2011). Pretreatment with a novel aquaporin 4 inhibitor, TGN-020, significantly reduces ischemic cerebral edema. Neurol Sci *32*, 113-116.

Isaacson, J.S. (1999). Glutamate spillover mediates excitatory transmission in the rat olfactory bulb. Neuron *23*, 377-384.

Jones, T.A., and Greenough, W.T. (1996). Ultrastructural evidence for increased contact between astrocytes and synapses in rats reared in a complex environment. Neurobiology of Learning and Memory *65*, 48-56.

Jourdain, P., Bergersen, L.H., Bhaukaurally, K., Bezzi, P., Santello, M., Domercq, M., Matute, C., Tonello, F., Gundersen, V., and Volterra, A. (2007). Glutamate exocytosis from astrocytes controls synaptic strength. Nature Neurosci *10*, 331-339.

Kaila, K., Price, T.J., Payne, J.A., Puskarjov, M., and Voipio, J. (2014). Cation-chloride cotransporters in neuronal development, plasticity and disease. Nature Rev Neurosci *15*, 637-654.

Kochlamazashvili, G., Henneberger, C., Bukalo, O., Dvoretskova, E., Senkov, O., Lievens, P.M., Westenbroek, R., Engel, A.K., Catterall, W.A., Rusakov, D.A., *et al.* (2010). The extracellular matrix molecule hyaluronic acid regulates hippocampal synaptic plasticity by modulating postsynaptic L-type Ca^{2+} channels. Neuron *67*, 116-128.

Korogod, N., Petersen, C.C.H., and Knott, G.W. (2015). Ultrastructural analysis of adult mouse neocortex comparing aldehyde perfusion with cryo fixation. Elife *4*.

Kullmann, D.M., and Asztely, F. (1998). Extrasynaptic glutamate spillover in the hippocampus: evidence and implications. Trends Neurosci *21*, 8-14.

Kullmann, D.M., Erdemli, G., and Asztely, F. (1996). LTP of AMPA and NMDA receptor-mediated signals: evidence for presynaptic expression and extrasynaptic glutamate spill-over. Neuron *17*, 461-474.

Lehre, K.P., and Danbolt, N.C. (1998). The number of glutamate transporter subtype molecules at glutamatergic synapses: Chemical and stereological quantification in young adult rat brain. J Neurosci *18*, 8751-8757.

Lehre, K.P., and Rusakov, D.A. (2002). Asymmetry of glia near central synapses favors presynaptically directed glutamate escape. Biophys J *83*, 125-134.

Liu, A., Zhou, Z.K., Dang, R., Zhu, Y.H., Qi, J.X., He, G.Q., Leung, C., Pak, D., Jia, Z.P., and Xie, W. (2016). Neuroligin 1 regulates spines and synaptic plasticity via LIMK1/cofilin-mediated actin reorganization. J Cell Biol *212*, 449-463.

Llano, O., Smirnov, S., Soni, S., Golubtsov, A., Guillemin, I., Hotulainen, P., Medina, I., Nothwang, H.G., Rivera, C., and Ludwig, A. (2015). KCC2 regulates actin dynamics in dendritic spines via interaction with beta-PIX. J Cell Biol *209*, 671-686.

Lozovaya, N.A., Kopanitsa, M.V., Boychuk, Y.A., and Krishtal, O.A. (1999). Enhancement of glutamate release uncovers spillover-mediated transmission by N-methyl-D-aspartate receptors in the rat hippocampus. Neurosci *91*, 1321-1330.

Luscher, C., Malenka, R.C., and Nicoll, R.A. (1998). Monitoring glutamate release during LTP with glial transporter currents. Neuron *21*, 435-441.

Lushnikova, I., Skibo, G., Muller, D., and Nikonenko, I. (2009). Synaptic potentiation induces increased glial coverage of excitatory synapses in CA1 hippocampus. Hippocampus *19*, 753-762.

Manabe, T., and Nicoll, R.A. (1994). Long-Term Potentiation - Evidence Against an Increase in Transmitter Release Probability in the Ca1 Region of the Hippocampus. Science *265*, 1888-1892.

Marvin, J.S., Borghuis, B.G., Tian, L., Cichon, J., Harnett, M.T., Akerboom, J., Gordus, A., Renninger, S.L., Chen, T.W., Bargmann, C.I., *et al.* (2013). An optimized fluorescent probe for visualizing glutamate neurotransmission. Nature Methods *10*, 162-170.

Matsuzaki, M., Ellis-Davies, G.C., Nemoto, T., Miyashita, Y., Iino, M., and Kasai, H. (2001). Dendritic spine geometry is critical for AMPA receptor expression in hippocampal CA1 pyramidal neurons. Nat Neurosci *4*, 1086-1092.

Matsuzaki, M., Honkura, N., Ellis-Davies, G.C., and Kasai, H. (2004). Structural basis of long-term potentiation in single dendritic spines. Nature *429*, 761-766.

Medvedev, N., Popov, V., Henneberger, C., Kraev, I., Rusakov, D.A., and Stewart, M.G. (2014). Glia selectively approach synapses on thin dendritic spines. Philos Trans R Soc Lond B Biol Sci *369*.

Medvedev, N.I., Popov, V.I., Rodriguez Arellano, J.J., Dallerac, G., Davies, H.A., Gabbott, P.L., Laroche, S., Kraev, I.V., Doyere, V., and Stewart, M.G. (2010). The N-methyl-D-aspartate receptor antagonist CPP alters synapse and spine structure and impairs long-term potentiation and long-term depression induced morphological plasticity in dentate gyrus of the awake rat. Neurosci *165*, 1170-1181.

Megevand, P., Troncoso, E., Quairiaux, C., Muller, D., Michel, C.M., and Kiss, J.Z. (2009). Long-term plasticity in mouse sensorimotor circuits after rhythmic whisker stimulation. J Neurosci *29*, 5326-5335.

Metcalf, D.J., Edwards, R., Kumarswami, N., and Knight, A.E. (2013). Test samples for optimizing STORM super-resolution microscopy. J Vis Exp.

Migliati, E., Meurice, N., DuBois, P., Fang, J.S., Somasekharan, S., Beckett, E., Flynn, G., and Yool, A.J. (2009). Inhibition of aquaporin-1 and aquaporin-4 water permeability by a derivative of the loop diuretic bumetanide acting at an internal pore-occluding binding site. Mol Pharmacol *76*, 105-112.

Min, M.Y., Rusakov, D.A., and Kullmann, D.M. (1998). Activation of AMPA, kainate, and metabotropic receptors at hippocampal mossy fiber synapses: role of glutamate diffusion. Neuron *21*, 561-570.

Min, R., and Nevian, T. (2012). Astrocyte signaling controls spike timing-dependent depression at neocortical synapses. Nat Neurosci *15*, 746-753.

Mishra, A., Reynolds, J.P., Chen, Y., Gourine, A.V., Rusakov, D.A., and Attwell, D. (2016). Astrocytes mediate neurovascular signaling to capillary pericytes but not to arterioles. Nature Neurosci *19*, 1619-1627.

Murai, K.K., Nguyen, L.N., Irie, F., Yamaguchi, Y., and Pasquale, E.B. (2003). Control of hippocampal dendritic spine morphology through ephrin-A3/EphA4 signaling. Nat Neurosci *6*, 153-160.

Nagelhus, E.A., and Ottersen, O.P. (2013). Physiological roles of aquaporin-4 in brain. Physiol Rev *93*, 1543-1562.

Nagerl, U.V., Eberhorn, N., Cambridge, S.B., and Bonhoeffer, T. (2004). Bidirectional activity-dependent morphological plasticity in hippocampal neurons. Neuron *44*, 759-767.

Navarrete, M., and Araque, A. (2010). Endocannabinoids potentiate synaptic transmission through stimulation of astrocytes. Neuron *68*, 113-126.

Nishida, H., and Okabe, S. (2007). Direct astrocytic contacts regulate local maturation of dendritic spines. J Neurosci *27*, 331-340.

Okubo, Y., Sekiya, H., Namiki, S., Sakamoto, H., Iinuma, S., Yamasaki, M., Watanabe, M., Hirose, K., and Iino, M. (2010). Imaging extrasynaptic glutamate dynamics in the brain. Proc Natl Acad Sci U S A *107*, 6526-6531.

Okumoto, S., Looger, L.L., Micheva, K.D., Reimer, R.J., Smith, S.J., and Frommer, W.B. (2005). Detection of glutamate release from neurons by genetically encoded surface-displayed FRET nanosensors. Proc Natl Acad Sci USA *102*, 8740-8745.

Oliet, S.H.R., Piet, R., and Poulain, D.A. (2001). Control of glutamate clearance and synaptic efficacy by glial coverage of neurons. Science *292*, 923-926.

Ostroff, L.E., Manzur, M.K., Cain, C.K., and Ledoux, J.E. (2014). Synapses lacking astrocyte appear in the amygdala during consolidation of Pavlovian threat conditioning. The Journal of comparative neurology *522*, 2152-2163.

Otmakhov, N., Khibnik, L., Otmakhova, N., Carpenter, S., Riahi, S., Asrican, B., and Lisman, J. (2004). Forskolin-induced LTP in the CA1 hippocampal region is NMDA receptor dependent. J Neurophysiol *91*, 1955-1962.

Panatier, A., Arizono, M., and Nagerl, U.V. (2014). Dissecting tripartite synapses with STED microscopy. Philos Trans R Soc Lond B Biol Sci *369*, 20130597.

Panatier, A., Theodosis, D.T., Mothet, J.P., Touquet, B., Pollegioni, L., Poulain, D.A., and Oliet, S.H. (2006). Glia-derived D-serine controls NMDA receptor activity and synaptic memory. Cell *125*, 775-784.

Panatier, A., Vallee, J., Haber, M., Murai, K.K., Lacaille, J.C., and Robitaille, R. (2011). Astrocytes are endogenous regulators of basal transmission at central synapses. Cell *146*, 785-798.

Papouin, T., Ladepeche, L., Ruel, J., Sacchi, S., Labasque, M., Hanini, M., Groc, L., Pollegioni, L., Mothet, J.P., and Oliet, S.H. (2012). Synaptic and extrasynaptic NMDA receptors are gated by different endogenous coagonists. Cell *150*, 633-646.

Pascual, O., Casper, K.B., Kubera, C., Zhang, J., Revilla-Sanchez, R., Sul, J.Y., Takano, H., Moss, S.J., McCarthy, K., and Haydon, P.G. (2005). Astrocytic purinergic signaling coordinates synaptic networks. Science *310*, 113-116.

Pereira, A.C., Lambert, H.K., Grossman, Y.S., Dumitriu, D., Waldman, R., Jannetty, S.K., Calakos, K., Janssen, W.G., McEwen, B.S., and Morrison, J.H. (2014). Glutamatergic regulation prevents hippocampal-dependent age-related cognitive decline through dendritic spine clustering. Proc Natl Acad Sci U S A *111*, 18733-18738.

Perez-Alvarez, A., Navarrete, M., Covelo, A., Martin, E.D., and Araque, A. (2014). Structural and functional plasticity of astrocyte processes and dendritic spine interactions. J Neurosci *34*, 12738-12744.

Peters, A., and Kaiserman-Abramof, I.R. (1970). The small pyramidal neuron of the rat cerebral cortex. The perikaryon, dendrites and spines. Am J Anat *127*, 321-355.

Popov, V., Medvedev, N.I., Davies, H.A., and Stewart, M.G. (2005). Mitochondria form a filamentous reticular network in hippocampal dendrites but are present as discrete bodies in axons: a three-dimensional ultrastructural study. J Comp Neurol *492*, 50-65.

Popov, V.I., Davies, H.A., Rogachevsky, V.V., Patrushev, I.V., Errington, M.L., Gabbot, P.L.A., Bliss, T.V.P., and Stewart, M.G. (2004). Remodelling of synaptic morphology but unchanged synaptic density during late phase long-term potentiation (LTP): A serial section electron micrograph study in the dentate gyrus in the anaesthetised rat. Neurosci *128*, 251-262.

Porter, J.T., and McCarthy, K.D. (1997). Astrocytic neurotransmitter receptors in situ and in vivo. Prog Neurobiol *51*, 439-455.

Reeves, A.M., Shigetomi, E., and Khakh, B.S. (2011). Bulk loading of calcium indicator dyes to study astrocyte physiology: key limitations and improvements using morphological maps. J Neurosci *31*, 9353-9358.

Rusakov, D.A. (2001). The role of perisynaptic glial sheaths in glutamate spillover and extracellular Ca^{2+} depletion. Biophys J *81*, 1947-1959.

Rusakov, D.A. (2015). Disentangling calcium-driven astrocyte physiology. Nature Rev Neurosci *16*, 226-233.

Rusakov, D.A., and Fine, A. (2003). Extracellular Ca^{2+} depletion contributes to fast activity-dependent modulation of synaptic transmission in the brain. Neuron *37*, 287-297.

Rusakov, D.A., Harrison, E., and Stewart, M.G. (1998). Synapses in hippocampus occupy only 1-2% of cell membranes and are spaced less than half-micron apart: a quantitative ultrastructural analysis with discussion of physiological implications. Neuropharmacol *37*, 513-521.

Rusakov, D.A., and Kullmann, D.M. (1998). Extrasynaptic glutamate diffusion in the hippocampus: ultrastructural constraints, uptake, and receptor activation. J Neurosci *18*, 3158-3170.

Rusakov, D.A., Kullmann, D.M., and Stewart, M.G. (1999). Hippocampal synapses: do they talk to their neighbours? Trends Neurosci *22*, 382-388.

Santello, M., Bezzi, P., and Volterra, A. (2011). TNFalpha controls glutamatergic gliotransmission in the hippocampal dentate gyrus. Neuron *69*, 988-1001.

Savtchenko, L.P., Bard, L., Jensen, T.P., Reynolds, J.P., Kraev, I., Medvedev, N., Stewart, M.G., Henneberger, C., and Rusakov, D.A. (2018). Disentangling astroglial physiology with a realistic cell model in silico. Nature Communications *9*, 3554.

Savtchenko, L.P., and Rusakov, D.A. (2005). Extracellular diffusivity determines contribution of high- versus low-affinity receptors to neural signaling. Neuroimage *25*, 101-111.

Savtchenko, L.P., Sylantyev, S., and Rusakov, D.A. (2013). Central synapses release a resource-efficient amount of glutamate. Nat Neurosci *16*, 10-12.

Scanziani, M., Salin, P.A., Vogt, K.E., Malenka, R.C., and Nicoll, R.A. (1997). Use-dependent increases in glutamate concentration activate presynaptic metabotropic glutamate receptors. Nature *385*, 630-634.

Schiapparelli, P., Guerrero-Cazares, H., Magana-Maldonado, R., Hamilla, S.M., Ganaha, S., Goulin Lippi Fernandes, E., Huang, C.H., Aranda-Espinoza, H., Devreotes, P., and Quinones-Hinojosa, A. (2017). NKCC1 Regulates Migration Ability of Glioblastoma Cells by Modulation of Actin Dynamics and Interacting with Cofilin. EBioMedicine, 10.1016/j.ebiom.2017.1006.1020.

Schiller, J., Major, G., Koester, H.J., and Schiller, Y. (2000). NMDA spikes in basal dendrites of cortical pyramidal neurons. Nature *404*, 285-289.

Schwab, A., Fabian, A., Hanley, P.J., and Stock, C. (2012). Role of ion channels and transporters in cell migration. Physiol Rev *92*, 1865-1913.

Scimemi, A., Fine, A., Kullmann, D.M., and Rusakov, D.A. (2004). NR2B-containing receptors mediate cross talk among hippocampal synapses. J Neurosci *24*, 4767-4777.

Shen, H.W., Scofield, M.D., Boger, H., Hensley, M., and Kalivas, P.W. (2014). Synaptic glutamate spillover due to impaired glutamate uptake mediates heroin relapse. J Neurosci *34*, 5649-5657.

Shepherd, G.M.G., and Harris, K.M. (1998). Three-dimensional structure and composition of CA3 -> CA1 axons in rat hippocampal slices: Implications for presynaptic connectivity and compartmentalization. J Neurosci *18*, 8300-8310.

Shigetomi, E., Jackson-Weaver, O., Huckstepp, R.T., O'Dell, T.J., and Khakh, B.S. (2013). TRPA1 channels are regulators of astrocyte basal calcium levels and long-term potentiation via constitutive D-serine release. J Neurosci *33*, 10143-10153.

Smith, A.C.W., Scofield, M.D., Heinsbroek, J.A., Gipson, C.D., Neuhofer, D., Roberts-Wolfe, D.J., Spencer, S., Garcia-Keller, C., Stankeviciute, N.M., Smith, R.J., *et al.* (2017). Accumbens nNOS Interneurons Regulate Cocaine Relapse. J Neurosci *37*, 742-756.

Svoboda, K., Tank, D.W., and Denk, W. (1996). Direct measurement of coupling between dendritic spines and shafts. Science *272*, 716-719.

Sykova, E., and Nicholson, C. (2008). Diffusion in brain extracellular space. Physiol Rev *88*, 1277-1340.

Sylantyev, S., Jensen, T.P., Ross, R.A., and Rusakov, D.A. (2013). Cannabinoid- and lysophosphatidylinositol-sensitive receptor GPR55 boosts neurotransmitter release at central synapses. Proc Natl Acad Sci U S A *110*, 5193-5198.

Szapiro, G., and Barbour, B. (2007). Multiple climbing fibers signal to molecular layer interneurons exclusively via glutamate spillover. Nature Neurosci *10*, 735-742.

Tanaka, M., Shih, P.Y., Gomi, H., Yoshida, T., Nakai, J., Ando, R., Furuichi, T., Mikoshiba, K., Semyanov, A., and Itohara, S. (2013). Astrocytic Ca2+ signals are required for the functional integrity of tripartite synapses. Molecular Brain *6*.

Thrane, A.S., Rappold, P.M., Fujita, T., Torres, A., Bekar, L.K., Takano, T., Peng, W.G., Wang, F.S., Thrane, V.R., Enger, R., *et al.* (2011). Critical role of aquaporin-4 (AQP4) in astrocytic Ca2+ signaling events elicited by cerebral edema. Proc Natl Acad Sci USA *108*, 846-851.

Tonnesen, J., Inavalli, V.V.G.K., and Nagerl, U.V. (2018). Super-resolution imaging of the extracellular space in living brain tissue. Cell *172*, 1108-1121.

Tonnesen, J., Katona, G., Rozsa, B., and Nagerl, U.V. (2014). Spine neck plasticity regulates compartmentalization of synapses. Nat Neurosci *17*, 678-685.

Tonnesen, J., Nadrigny, F., Willig, K.I., Wedlich-Soldner, R., and Nagerl, U.V. (2011). Two-color STED microscopy of living synapses using a single laser-beam pair. Biophys J *101*, 2545-2552.

Tradtrantip, L., Jin, B.J., Yao, X., Anderson, M.O., and Verkman, A.S. (2017). Aquaporin-Targeted Therapeutics: State-of-the-Field. Adv Exp Med Biol *969*, 239-250.

Tsvetkov, E., Shin, R.M., and Bolshakov, V.Y. (2004). Glutamate uptake determines pathway specificity of long-term potentiation in the neural circuitry of fear conditioning. Neuron *41*, 139-151.

Ventura, R., and Harris, K.M. (1999). Three-dimensional relationships between hippocampal synapses and astrocytes. J Neurosci *19*, 6897-6906.

Vogt, K.E., and Nicoll, R.A. (1999). Glutamate and gamma-aminobutyric acid mediate a heterosynaptic depression at mossy fiber synapses in the hippocampus. Proc Natl Acad Sci USA *96*, 1118-1122.

Volterra, A., Liaudet, N., and Savtchouk, I. (2014). Astrocyte Ca^{2+} signalling: an unexpected complexity. Nat Rev Neurosci *15*, 327-335.

Watkins, S., and Sontheimer, H. (2011). Hydrodynamic cellular volume changes enable glioma cell invasion. J Neurosci *31*, 17250-17259.

Wenzel, J., Lammert, G., Meyer, U., and Krug, M. (1991). The influence of long-term potentiation on the spatial relationship between astrocyte processes and potentiated synapses in the dentate gyrus neuropil of rat-brain. Brain Res *560*, 122-131.

Whitfield, J.H., Zhang, W.H., Herde, M.K., Clifton, B.E., Radziejewski, J., Janovjak, H., Henneberger, C., and Jackson, C.J. (2015). Construction of a robust and sensitive arginine biosensor through ancestral protein reconstruction. Protein Science *24*, 1412-1422.

Yasuda, R., Sabatini, B.L., and Svoboda, K. (2003). Plasticity of calcium channels in dendritic spines. Nat Neurosci *6*, 948-955.

Zheng, K., Bard, L., Reynolds, J.P., King, C., Jensen, T.P., Gourine, A.V., and Rusakov, D.A. (2015). Time-resolved imaging reveals heterogeneous landscapes of nanomolar Ca^{2+} in neurons and astroglia. Neuron *88*, 277-288.

Zheng, K., Scimemi, A., and Rusakov, D.A. (2008). Receptor actions of synaptically released glutamate: the role of transporters on the scale from nanometers to microns. Biophys J *95*, 4584-4596.

STAR METHODS

CONTACT FOR REAGENT AND RESOURCE SHARING

Further information and requests for resources and reagents should be directed to the Lead Contact Dmitri Rusakov (d.rusakov@ucl.ac.uk).

EXPERIMENTAL MODEL AND SUBJECT DETAILS

Animals

All animal procedures were conducted in accordance with the European Commission Directive (86/609/ EEC), the United Kingdom Home Office (Scientific Procedures) Act (1986), and all relevant national (France, Germany) and institutional guidelines. Details on each of the animal models employed are given throughout the text and summarized below. All animals were maintained in controlled environments as mandated by national guidelines, on 12hr light/dark cycles, with food and water provided *ab libitum*.

For *ex vivo* electrophysiology and imaging, a combination of Wistar rats (3 – 5 weeks old, male), Sprague-Dawley rats (3 – 5 weeks old, male), KO and transgenic mice (3 – 5 weeks old, male) were employed. For experiments requiring viral-mediated expression of optical sensors, male and female wildtype C57BL/6 mice (Charles River Laboratories) were injected at 3 - 4 weeks of age with viral vectors and acute slices were obtained 2 – 4 weeks later. AQP KO mice were backcrossed with C57BL/6 mice for five generations before intercrossing to yield KO (-/-) and wildtype (+/+) mice.

For STED microscopy, organotypic hippocampal slice cultures were prepared from 5 – 7 day old Thy1-YFP mice.

For *in vivo* recordings, group-housed male and female wildtype C57BL/6 mice (Charles River Laboratories) were used. Animals served as their own controls through the use of ipsi- and contralateral stimuli as specified below. All animals were injected with viral vectors at 3 – 4 weeks, and cranial windows were implanted 2 weeks later. Imaging was performed at between 6 and 12 weeks of age, at least 3 weeks after injection of viral vectors.

METHOD DETAILS

Preparation of acute slices

350 μm thick acute hippocampal slices were obtained from three- to five week-old male Sprague-Dawley, Wistar rats, wild-type, knockout and transgenic mice (specified below). Slices were prepared in an ice-cold slicing solution containing (in mM): NaCl 75, sucrose 80, KCl 2.5, $MgCl_2$ 7, NaH_2PO_4 1.25, $CaCl_2$ 0.5, $NaHCO_3$ 26, ascorbic acid 1.3, sodium pyruvate 3, and glucose 6 (osmolarity 300-305), stored in the slicing solution at 34°C for 15 minutes before being transferred to an interface chamber for storage in an extracellular solution containing (in mM): NaCl 126, KCl 2.5, $MgSO_4$ 1.3, NaH_2PO_4 1, $NaHCO_3$ 26, $CaCl_2$ 2, and glucose 10 (pH 7.4, osmolarity adjusted to 295-305). All solutions were continuously bubbled with 95% O_2/ 5% CO_2. Slices were allowed to rest for at least 60 minutes before recordings started. For recordings, slices were transferred to the submersion-type recording chamber and superfused, at 33-35°C unless shown otherwise. Where required, 50-100 μM picrotoxin and 5 μM CGP52432 were added to block GABA receptors and a cut between CA3 and CA1 was made to suppress epileptiform activity.

Electrophysiology *ex vivo*

Electrophysiological examination of astrocytes was carried out as previously described (Henneberger et al., 2010; Henneberger and Rusakov, 2012). Briefly, whole-cell recordings in astrocytes were obtained using standard patch pipettes (3-4 MΩ) filled with an intracellular solution containing (in mM) KCH_3O_3S 135, HEPES 10, Na_2-Phosphocreatine or di-Tris-Phosphocreatine 10, $MgCl_2$ 4, Na_2-ATP 4, Na-GTP 0.4 (pH adjusted to 7.2 using KOH, osmolarity 290-295). Cell-impermeable dyes Fluo-4 (200 µM, Invitrogen) and Alexa Fluor 594 hydrazide (20-100 µM) or Texas Red Dextran (100 µM, Invitrogen) were routinely added to the intracellular solution, unless indicated otherwise. Where specified, bumetanide (20 µM) or S3 peptide fragment (200 µM, Anaspec) was added to the intracellular solution. Passive astrocytes were identified by their small soma size (~10 µm; visualized in the Alexa emission channel), low resting potential (below -80 mV without correction for the liquid-junction potential), low input resistance (< 10 MΩ), passive (ohmic) properties and characteristic morphology of the arbor (Fig. 1 and Fig. S1). Astrocytes were either held in voltage clamp mode at their resting membrane potential or in current clamp. Where specified, the intracellular free Ca^{2+} concentration was clamped to a steady-state level of 50-80 nM by adding 0.45 mM EGTA and 0.14 mM $CaCl_2$ to the intracellular solution (calculation by WebMaxChelator, Stanford).

LTP induction *ex vivo*

Where indicated, an extracellular recording pipette was placed immediately adjacent to the astrocyte under investigation visualized in the Alexa channel (Fig. 1). Synaptic responses were evoked by orthodromic stimulation (100 µs, 20-100 µA) of Schaffer collaterals using either a bipolar or coaxial stimulation electrode placed in the *stratum radiatum* >200 µm away from the recording electrodes. Field EPSPs (fEPSPs) were recorded using a standard patch pipette filled with the extracellular solution. Predominantly AMPAR-mediated fEPSPs (with no NMDAR blockers added) are denoted AMPAR fEPSPs throughout the text. In some experiments, astrocytic field EPSPs (a-fEPSPs) were also recorded using the cell patch pipette (Henneberger and Rusakov, 2012): the latter readout was fully consistent with extracellular fEPSPs (Fig. S4C). The baseline stimulus intensity was set at ~50% of the maximal response, stimuli were applied every 30 seconds for at least 10 minutes before LTP was induced using three trains of high-frequency stimulation (HFS, 100 pulses at 100 Hz) 60 seconds apart. The slope of fEPSPs was monitored afterwards for at least 30 minutes. See sections below for LTP induction protocols used in specific experiments, such as through glutamate uncaging or using a 'chemical cocktail'.

Two-photon excitation imaging of astroglia *ex vivo*

We used a Radiance 2100 (Zeiss-Biorad), FV10MP (Olympus), Femto3D-RC or Femto2D (Femtonics, Budapest) and a Scientifica imaging system optically linked to femtosecond pulse lasers MaiTai (SpectraPhysics-Newport) or Vision S (Coherent) and integrated with patch-clamp electrophysiology. Once in whole-cell mode, dyes normally equilibrated across the astrocyte tree within 5-10 min. Routinely, in astrocyte morphology time-lapse experiments astrocytes loaded with fluorescence indicators (see above) were imaged in frame mode at a nominal resolution of ~ 0.1 µm / pixel (512x512 pixels, 25x Olympus objective /NA1.05) in the red emission channel (540LP / 700SP filter; λ_x^{2P} = 800 nm). To minimize photodamage only a single focal section through the soma (average of three) was acquired at a laser intensity of 3-6 mW under the objective with careful adjustment of the z-position.

iGluSnFR transduction of hippocampal astroglia and neurons

*Stereotactic injections: astroglial expression of iGluSnFR***.** For the expression of the glutamate sensor iGluSnFR (Marvin et al., 2013) in astrocytes, an AAV virus expressing iGluSnFR under a GFAP promoter (AAV1.GFAP.iGluSnFr.WPRE.SV40, Penn Vector Core, PA, USA) was injected bilaterally into the ventral hippocampus. C57BL6/N mice (4 weeks old, Charles Rivers Laboratories) were injected intra-peritoneally with a ketamin/medotomidine anaesthesia (100 and 0.25 mg per kg body weight in NaCl, injection volume 0.1 ml per 10 g body weight, ketamin 10%, betapharm; Cepotir 1 mg/ml, CPPharma). Firstly, the head fur was removed and the underlying skin disinfected. After ensuring that the animal was under deep anesthesia, the head was fixed in a stereotactic frame (Model 901, David Kopf Instruments). After making an incision, bregma was localized. Next, the coordinates for the ventral hippocampus (relative to bregma: anterior -3.5 mm, lateral -/+3 mm, ventral -2.5 mm) were determined and the skull was locally opened with a dental drill. Under control of a micro injection pump (100 nl/min, WPI) 1 µl viral particles were injected with a beveled needle nanosyringe (nanofil 34G BVLD, WPI). After retraction of the syringe, the incision was sutured using absorbable thread (Ethicon). Finally, the anesthesia was stopped by i.p. application of atipamezol (2.5 mg per kg body weight in NaCl, injection volume 0.1 ml per 10 g body weight, antisedan 5 mg/ml, Ventoquinol). To ensure analgesia, carprofen (5 mg/kg in NaCl, injection volume 0.1 ml/20 g body weight, Rimadyl 50 mg/ml, Zoetis) was injected subcutaneously directly, 24h and 48h after the surgery.

*Stereotactic injections: neuronal expression of iGluSnFR***.** C57BL/6 mice (3 - 4 weeks of age), male and female, were prepared for aseptic surgery and anaesthetised using isoflurane (5% v/v induction, 1.5 - 2.5% maintenance). The scalp was shaved and disinfected using three washes of topical chlorhexidine. The animal was secured in a stereotaxic frame (David Kopf Instruments, CA, USA) and loss of pedal reflexes was confirmed prior to surgery. Body temperature was maintained at 37.0 ± 0.5 °C using a feedback rectal thermometer and heating blanket. Perioperative analgesics were administered (subcutaneous buprenorphine, 60 µg kg-1, topical lidocaine/prilocaine emulsion, 2.5%/2.5%) before ocular ointment (Lacri-lube, Allergan, UK) was applied to the eyes. A small midline incision was made and superficial tissue resected to expose the skull. A craniotomy of approximately 1 - 2 mm diameter was performed over the right hemisphere using a high-speed hand drill (Proxxon, Föhren, Germany), at a site overlying the medial hippocampus. Stereotactic coordinates were 60 % of the anteroposterior distance from bregma to lambda and 2.5 mm lateral to midline. Upon exposure, a warmed, sterile saline solution was applied to exposed cortical surface during the procedure.

Pressure injections of AAV9 hSyn iGluSnFR (totalling 0.1 - 1 x 1010 genomic copies in a volume not exceeding 200 nL, supplied by Penn Vector Core, PA, USA) were carried out using a pulled glass micropipette stereotactically guided to a depth of 1.3 mm beneath the cortical surface, at a rate of approximately 1 nL sec-1. The total injection volume was delivered in three steps, reducing depth by 100 µm at each step. Once delivery was completed, pipettes were left in place for 5 minutes before being retracted. The surgical wound was closed with absorbable 7-0 sutures (Ethicon Endo-Surgery GmbH, Norderstedt, Germany) and the animal was left to recover in a heated chamber. Meloxicam (subcutaneous, 1 mg kg-1) was subsequently administered once daily for up to two days following surgery. Mice were killed by transcardial perfusion with ice-cold sucrose-enriched slicing medium (in mM, 105 sucrose, 60 NaCl, 2.5 KCl, 1.25 NaH2PO4, 26 NaHCO3, 15 glucose, 1.3 ascorbic acid, 3 Na pyruvate, 0.5 CaCl2 and 7 MgCl2, saturated with 95% O2 and 5% CO2) after a 2 - 4 week AAV incubation period

and acute hippocampal slices prepared for imaging and electrophysiological recordings as below.

Viral transduction of thalamocortical boutons and astrocytes in the barrel cortex

C57BL/6 mice (3 - 4 weeks of age), male and female, were prepared as above for neuronal expression of iGluSnFR. During the procedure, two craniotomies of approximately 1 - 2 mm diameter were performed over the right hemisphere using a high-speed hand drill (Proxxon, Föhren, Germany), at sites overlying the ventral posteromedial nucleus of the thalamus (VPM) and the barrel cortex (S1BF). The entire microinjection into the VPM was completed prior to performing the second craniotomy over S1BF. Stereotactic coordinates for VPM injections were -1.8 mm and 1.5 mm along the anteroposterior and mediolateral axes, respectively. Two injection boluses was delivered at 3.0 and 3.2 mm beneath the dural surface. For S1BF injections, the coordinates were -0.5 mm and 3.0 mm along the anteroposterior and mediolateral axes, respectively, delivering a single bolus at a depth of 0.6 mm. A warmed saline solution was applied to exposed cortical surface during the procedure.

Pressure injections of AAV9 hSyn.GCaMP6f (totalling 1 x 1010 genomic copies in a volume not exceeding 200 nL, supplied by Penn Vector Core, PA, USA) and AAV5 GfaABC1D tdTomato (0.5 x 1010 genomic copies, in a volume not exceeding 200 nL, supplied by Penn Vector Core, PA, USA) were carried out using a glass micropipette at a rate of 1 nL sec-1, stereotactically guided to the VPM and S1BF, respectively, as outlined above. Once delivery was completed, pipettes were left in place for 5 minutes before being retracted. The surgical wound was closed and the animal recovered as outlined above for neuronal expression of iGluSnFr. Meloxicam (subcutaneous, 1 mg kg-1) was administered once daily for up to two days following surgery. Mice were subsequently prepared for cranial window implantation approximately 2 weeks later.

Cranial window implantation

Mice were prepared for aseptic surgery and secured in a stereotaxic frame as before during the viral transduction procedure. Once secured and under stable anaesthesia (isoflurane, maintenance at 1.5 - 2%), a large portion of the scalp was removed to expose the right frontal and parietal bones of the skull, as well as the medial aspects of the left frontal and parietal bones. The right temporalis muscles were reflected laterally to expose the squamous suture, to facilitate cement bonding during fixation of the cranial window implant. The exposed skull was coated with Vetbond (3M, MN, USA) and a custom-made headplate was affixed over the S1BF. The assembly was then secured with dental cement (SuperBond, Sun Medical Co. Ltd., Japan). Once the bonding agents had cured, the animal was removed from the stereotaxic frame and it's headplate was secured in a custom-built head fixation frame. A craniotomy of approximately 4 mm diameter was carried out over the right somatosensory cortex, centred over the S1BF injection site. Immediately prior to removal of the skull flap, the surface was superfused with warmed aCSF (in mM; 125 NaCl, 2.5 KCl, 26 NaHCO3, 1.25 Na2HPO4,18 Glucose, 2 CaCl2, 2 MgSO4; saturated with 95% O2 / 5% CO2, pH 7.4). The dura was resected using a combination of 26G needles (tapped against a hard surface to introduce a curved profile), fine-tipped forceps (11252-40, Fine Science Tools, Germany) and 2.5 mm spring scissors (15000-08, Fine Science Tools, Germany), taking care not to penetrate to the pia mater. Once the dura was removed, a previously-prepared coverslip consisting of a 34 mm diameter round coverglass affixed beneath a 4 mm diameter round coverglass (Harvard Apparatus UK, affixed using a UV-curable optical adhesive (NOA61), ThorLabs Inc., NJ, USA) was placed over the exposed cortex. Slight downward pressure was applied to the

coverslip using a stereotactically guided wooden spatula that was previously severed and sanded to allow some flexibility and preclude excessive force. The superfusion was discontinued and excess aCSF was removed using a sterile surgical sponge, taking care not to wick fluid from beneath the cranial window. The coverslip was then secured with VetBond and dental cement, sequentially. Once cured, the animal was recovered in a heated chamber and returned to its homecage when ambulatory. Post-operative care was administered as before during the viral transduction procedure.

Multiphoton imaging *in vivo*

Two-photon excitation was carried out using a wavelength multiplexing suite consisting of a Newport-Spectraphysics Ti:sapphire MaiTai tunable IR laser pulsing at 80 MHz and a Newport-Spectraphysics HighQ-2 fixed-wavelength IR laser pulsing at 63 MHz. The laser lightpaths were aligned (though not synchronised) before being point-scanned using an Olympus FV1000 with XLPlan N 25x water immersion objective (NA 1.05). During imaging, animals were lightly anaesthetised (fentanyl, 0.03 mg kg-1, midazolam, 3 mg kg-1, and medetomidine, 0.3 mg kg-1) and secured under the objective on a custom-built stage via the previously affixed headplate.

Initial acquisitions were performed with both lasers illuminating the tissue at 910 nm and 1040 nm, respectively, in order to locate active thalamocortical boutons in S1BF within the arbor of tdTomato-positive cortical astrocytes. Brief 5 second, 3 Hz pulses of nitrogen were directed at the contralateral whiskers to determine responsive regions of interest. Measurements were performed in L1 and L2/3, at depths of 50 - 150 nm. For bouton recordings, framescans of 4 - 20 Hz were performed, with a pixel dwell time of 2 μs and a mean laser power of 30 mW at the focal plane. Upon identification of suitable astrocytes, we sampled the baseline VF. Except when needed for illustrative purposes, illumination by the tunable IR laser (910 nm, to excite GCaMP6f) was occluded at this stage, in order to limit photobleaching. High-resolution z-stacks, incorporating 1 or more astrocytes, were taken every 2.5 minutes, for 15 - 20 minutes. Z-stacks were 512 x 512 pixels, with a pixel size of 0.25 - 0.5 μm and an interval size of 1.5 - 2.5 μm. Sensory-evoked synaptic potentiation within the barrel cortex was then induced as previously described (Gambino et al,. 2014), via a contralateral rhythmic whisker stimulation (RWS, 120 sec, 3 Hz). Sampling of z-stacks, covering the same cortical area, was continued for 30 - 45 minutes following the RWS. The same regions were sampled again one week later, before and after an ipsilateral RWS, to serve as control VF measurements. To determine VF in vivo, stacks were coded (to blind experimenters) and motion-corrected using MATLAB. Fluorescence values for the astrocytic soma and 2 - 4 ROIs within its arbor, from the same focal plane, were tabulated. Sampling of fluorescence from the primary astrocytic branches was avoided as pilot data indicated that VF changes within such branches was negligible. Values for each ROI were averaged to give cell-specific ratiometric fluorescence values, which were normalized to yield relative changes in VF.

Monitoring astrocyte tissue volume fraction

Astrocyte tissue volume fraction (VF) was monitored to detect structural changes of fine astrocyte branches smaller than the diffraction limit (200-300 nm for diffraction-limited 2PE imaging). VF was obtained by normalizing the background-corrected fluorescence of the morphological dye Alexa Fluor 594 or Texas Red Dextran to somatic values, where 100% of the tissue is occupied by the astrocyte (Fig. 1A-B, Fig. S1A-C). The VF values obtained with this approach were not affected by dye escape through gap-junctions or hemichannels (Fig. S1C).

Image segmentation measure to gauge astrocyte morphology

The astrocyte VF directly reflects the number and average size of all astrocyte processes in the imaged focal plane. Changes of either cannot be differentiated by the VF measurements alone. To identify further parameters reflecting astrocyte morphology changes, we used Monte Carlo simulations of the diffraction-limited imaging of astrocyte processes in a focal plane by mimicking a typical experimental scenario. Non-overlapping virtual astrocyte processes, represented by rectangular cuboids, were simulated randomly in a 3D focal plane (2000 x 2000 x 80 voxels, voxel size 25 x 25 x 25 nm), and 'projected' onto the *x-y* plane by averaging along the z-axis. They were resampled at imaging resolution (100 nm/pixel) and convolved with a point-spread-function (PSF) fit to experimentally determined PSFs (fluorescent beads, 175 and 40 nm, Invitrogen), as illustrated by Fig. S1D. A set of images was generated by randomly varying the numbers and sizes of simulated astrocyte processes (Visual Studio C++, OpenCV image processing library) and analysed. The VF values scaled directly with the number of astrocytes processes in the simulated focal plane and their average size. We therefore set out to calculate astrocyte image segmentation parameter, a VF-independent indicator of astrocyte process number and size. Segmentation was calculated by (a) applying a variable binary threshold to the image (which was scaled in the original grey-level brightness values), (b) performing a particle count, and (c) repeating the procedure for the threshold values covering the entire brightness range. The maximum number of particles counted over all thresholds thus represented the segmentation value used for further analyses (Fig. 1G).

In our Monte Carlo simulations, lower segmentation values indicated either a decrease in simulated astrocyte process numbers or an increase in the average astrocyte process volume (Fig. S1D-F), or a combination of the two; an increase represented the opposite. In combination, changes of VF and segmentation parameters should indicate whether the astrocyte process number and/or average volume have changed in the observed focal plane (Fig. S1G). To relate these predictions to empirical data, we also induced swelling and shrinkage of astrocyte processes by reducing or increasing the osmolarity, respectively, of the extracellular solution (to either 220 mOsm or 420 mOsm, for 10 minutes). Thus, the experimental segmentation data were consistent with the suggestion that LTP induction reduces the number of discernable cell compartments while decreasing the overall VF (Fig. S1G).

Image entropy measurement

The image entropy parameter (Fanelli et al., 2011) was calculated as $-\sum p_i * ln(p_i)$ where p_i stands for the count (proportion) of pixels at the *i*th brightness level in the original brightness scale (natural logarithm was used for scaling purposes). Image analyses of experimental data were performed in Matlab (Mathworks). Testing the relationship between entropy and other imaging characteristics was carried out using Monte Carlo simulated populations of astroglial processes, as described.

Fluorescence recovery after photobleaching (FRAP) experiments

FRAP of Alexa Fluor 594 was used to quantify changes of intracellular diffusivity in astrocytes. Fluorescence recordings were obtained in line-scan mode (500 Hz, line placed quasi-randomly through the astrocyte arbour) at an increased laser power of 15-20 mW under the objective to induce substantial bleaching of Alexa Fluor 594.

Optical measurements of extracellular diffusivity

The effective diffusivity of fluorescent dyes was determined using a point-source diffusion method as previously described (Savtchenko and Rusakov, 2005; Zheng et al., 2008). Briefly, a bolus of fluorescent dye (Alexa Fluor 594 hydrazide, 50 µM in extracellular solution) was ejected from a patch pipette into the CA1 *stratum radiatum* neuropil by a pressure pulse (0.8 bar, 2-6 ms). The diffusion spread of the dye was traced by scanning along a line in front of the ejection pipette (~300-1000 Hz; Fig. S2A). Fluorescence life profiles for each time point were fitted with a Gaussian function $\exp((x - xc)^2/(4\ w))$ with $w = D_{eff}\ t$ where x is the position within the linescan, xc the puff position, D_{eff} the effective diffusivity and t the time since the puff. D_{eff} is then obtained by linear fitting of w(t) (Fig. S2B). All analyses were performed using Matlab (Mathworks). Measurements were repeated every 10 minutes. Field EPSPs were evoked by Schaffer collateral stimulation (see above) and recorded through another field pipette less than 150 µm away from the puff pipette. In a subset of recordings LTP was induced after 10 minutes of baseline recording.

STED microscopy in organotypic slices

Organotypic hippocampal slice cultures were prepared from 5-7 day pups of Thy1-YFP transgenic mice in accordance with the French National Code of Ethics on Animal Experimentation and approved by the Committee of Ethics of Bordeaux (No. 50120199). As described before (Nagerl et al., 2004), cultures were prepared using the roller tube method (Gähwiler method). First, pups were decapitated. Then, brains were removed, hippocampus dissected (in cooled Gey's Balanced Salt Solution, GBSS) and 350 µm coronal slices were sectioned using a tissue chopper (McIlwain). After 30-60 minutes rest at 4°C in GBSS, each half slice was mounted on a glass coverslip coated with heparinized chicken plasma (10 µl, Sigma). Thrombin (Merck) was added to coagulate the plasma and to allow the slice to adhere to the coverslip. After 30 minutes at room temperature, each coverslip was inserted into a delta tube (Nunc) before adding 750 µl culture medium containing: 50% Basal Medium Eagle (BME, Gibco), 25% Hanks' Balanced Salt solution (HBSS, Gibco), 25% of heat inactivated horse serum (Gibco) supplemented with glutamine to a final concentration of 1mM and glucose to a final concentration of 11g/l (Sigma). Finally, slices were cultivated during 5-6 weeks in tubes placed on a roller-drum incubator set at 35 °C in dry air with a rotation rate of ~10 revolutions per hour. The experimental day, the slice was transferred to a submersion-type recording chamber perfused (2 ml/min) with ACSF at 31°C saturated with 95%O_2/5%CO_2 and containing (in mM): NaCl 119, KCl 2.5, NaH2PO4 1.25, NaHCO3 26, Trolox 1.5 and 10 glucose (pH 7.4; osmolarity 295-298) in the presence of 1.3 mM Mg^{2+} and 2 mM Ca^{2+}.

To enable STED microscopy studies, as described previously (Tonnesen et al., 2011), our home-built STED microscope was constructed around the base of an inverted confocal microscope (DMI 6000 CS Trino, Leica, Mannheim, Germany) using a glycerin objective with a high numerical aperture and equipped with a correction color (PL APO, CORR CS, 63x, NA 1,3; Leica), providing an optical resolution of at least 70 nm in x-y tens up to 50 µm below the tissue surface. A pulsed-laser diode (PDL 800-D, Picoquant, Berlin, Germany) was used to deliver excitation pulses at 485 nm wavelength with 90 ps duration. Furthermore, an optical parametric oscillator (OPO BASIC Ring fs RTP, APE, Berlin, Germany) pumped by a Ti:Sapphire laser (MaiTai, Spectra-Physics, Darmstadt, Germany), operating at 80 MHz produced a pulsed STED beam centered at a wavelength of 592 nm, to quench the fluorescence. The maximal power of the STED beam going into the back aperture of the objective was 12 mW. Both, excitation and STED pulses were synchronized at 80 MHz by externally triggering the laser diode and optimizing the relative delay using an electronic delay generator. The fluorescence signal was first separated from the excitation light by a dichroic

mirror (499-nm long-pass), then cleaned with a 525/50 band-pass filter, spectrally separated by a dichroic mirror (514-nm long-pass), and finally imaged onto two multimode optical fibers connected to avalanche photodiodes (SPCM-AQR-13-FC, PerkinElmer, Waltham, MA).

Image acquisition was controlled by the custom-written software IMSpector (www.max-planck-innovation.de/de/industrie/technologieangebote/software/). The pixel dwell time was 15 µs with a pixel size of 19.53 nm. Typically, 2 µm stacks, with nine z-sections, 220 nm apart were acquired. As described before (Tonnesen et al., 2011), YFP (in neurons) and Alexa Fluor 488 (in astrocytes) were spectrally detected using a 514 nm long-pass emission filter. Effective color separation was achieved offline by linear un-mixing of the fluorescence channels (using a plugin from ImageJ) after deconvolution (3 iterations) using Huygens Professional (SVI). All morphometric analyses were done on deconvolved image sections of the two unmixed color channels. To determine spine head width, a 3-pixel thick line was manually positioned through the largest part of the spine head, and the full width at half maximum (FWHM) as a measure of spine size was extracted from the line profile. Astrocytic processes and spines were considered to be in close proximity if the visible distance between their edges (as determined by the FWHM of a line profile laid across the point of shortest distance) was equal or less than 20 nm, corresponding to one pixel. Conversely, for separations larger than 1 pixel, the astrocytic process and spine were not considered to be in close proximity.

Fast fixation and DAB staining of recorded astrocytes

In a subset of experiments, we loaded an astrocyte with biocytin, and after the experiment the slices were rapidly fixed (by submersion) with 1.25% glutaraldehyde and 2.5% paraformaldehyde in 0.1 M PB (phosphate buffer, pH 7.4), to be kept overnight, infiltrated in 10% sucrose in PB for 10 min and then in 20 % sucrose in PB for 30 min. Infiltrated slices were consequentially freeze-thaw in liquid freon and liquid nitrogen for 3 sec each to gently crack intracellular membranes and embedded in 1% low gelling temperature agarose in PB (Sigma-Aldrich, USA). Embedded slices were sectioned at 50 µm on a vibrating microtome (VT1000; Leica, Milton Keynes, UK). 50 µm sections were incubated in 1% H2O2 in PB for 20 min to eliminate blood background, washed with 0.1 M TBS (tris buffer saline, pH 7.4) and incubated with ABC solution (VECTASTAIN ABC, Vector laboratories, USA) for 30 min at room temperature. Next section were washed with 0.1M TB (tris buffer, pH 7.4), pre-incubated with DAB (3,3'-Diaminobenzidine tablets - Sigma-Aldrich, USA) solution (10 mg DAB tablet + 40 ml TB) for 30 min at room temperature in dark and finally incubated with DAB+ H2O2 solution (5 µl of 33% H2O2 + 25 ml of DAB solution) for 10-20 min at room temperature in dark. The DAB stained sections were washed in PB, post-fixed in 2% osmium tetroxide and further processing and embedding protocols were essentially similar to those reported previously (Medvedev et al., 2010). Briefly, the tissue was dehydrated in graded aqueous solutions of ethanol (30-100%) followed by 3 times in 100% acetone, infiltrated with a mixture of 50% epoxy resin (Epon 812／Araldite M) and 50% acetone for 30 min at room temperature, infiltrated in pure epoxy resin, and polymerized overnight at 80 °C. Sections in blocks were coded and all further analyses were carried out blind as to the experimental status of the tissue.

3D electron microscopy

Serial sections (60–70 nm thick) were cut with a Diatome diamond knife as detailed and illustrated earlier (Medvedev et al., 2010; Popov et al., 2005; Popov et al., 2004), and systematically collected using Pioloform-coated slot copper grids (each series consisted of up to 100 serial sections). Sections were counterstained with 4% uranyl acetate, followed by lead

citrate. Finally sections were imaged in *stratum radiatum* area of CA1 (hippocampus) using an AMT XR60 12 megapixel camera in a JEOL 1400 electron microscope. Serial sections were aligned as JPEG images using SEM align 1.26b (software available from http://synapses.clm.utexas.edu/). 3D reconstructions of DAB stained astrocyte processes and the adjacent dendritic spines were performed in Trace 1.6b software (http://synapses.clm.utexas.edu/). Dendritic spines were categorized according to (Harris et al., 1992; Peters and Kaiserman-Abramof, 1970); since 90-95% of excitatory synapses in CA1 area of hippocampus are located on either thin or mushroom dendritic spines only the mushroom (n = 88) and thin (n = 243) spines were reconstructed and analyzed. 3D reconstructions of segmented astrocytic processes and dendritic spines were imported to 3D-Studio-Max 8 software for rendering of the reconstructed structures.

Measurements of astroglial coverage in 3D EM

To analyze the astroglial coverage of synapses, a set of virtual 100 nm thick concentric spherical shells (Fig. 3D) was arranged *in silico* around each reconstructed PSD using custom-made software. The volume of each shell as well as the volume and surface area of astrocytic segments inside each shell were computed to estimate the volume fraction (VF) occupied by astrocyte processes (astrocyte volume / total shell volume) and the surface area of astrocyte, throughout concentric shell between centered at 0-0.5 μm around the centroid of each individual PSD. In some cases, we also carried out additional analyses using curvilinear 3D shells reproducing the contours of each PSD; the results were qualitatively identical. All data from digital reconstructive analyses were evaluated to obtain one value for each individual slice taken from individual animals (there were n = 3 preparations in each group), in each data set. ANOVA tests were used to examine differences between specific animal groups (implemented through Origin Pro 7.5). Data were presented as mean ± SEM (n = 3 animals per group).

Immunohistochemistry and three-color 3D dSTORM

We used a modified protocol described by us previously (Heller et al., 2017). Deeply anaesthetized rats (Sprague Dawley, ~500 g) were perfused with ice-cold 4% PFA in PBS, brains were removed and incubated in 4% PFA in PBS overnight at 4°C; 30 μm coronal sections were prepared and kept free-floating in PBS; non-reacted aldehydes were quenched in 0.1% $NaBH_4$ in PBS for 15 min; washed thrice for 5 min with PBS; autofluorescence was quenched with 10 mM $CuSO_4$ in 50 mM NH_4Cl, final pH = 5 for 10 min; washed with H_2O thrice quickly and once with PBS (5 min). Permeabilisation and blocking was carried out with PBS-S (0.2% saponin in PBS) supplemented with 3% BSA for at least 3 hours; incubated with primary antibody (see below) in PBS-S overnight at 4°C; washed trice with PBS-S; incubated with secondary antibody (see below) in PBS-S for two hours; washed with PBS-S twice for 10 min and with PBS twice for 10 min; post-fixed with 4% PFA in PBS for 30 min; washed with PBS thrice for 10 min; incubated in Scale U2 buffer (Hama et al., 2011) (4 M urea, 30% Glycerol and 0.1% Triton X-100 in water) at 4°C until being prepared for imaging.

Primary antibodies were for: presynaptic protein Bassoon (Mouse, SAP7F407, Recombinant rat Bassoon, Novus, NB120-13249, AB_788125, dilution 1:500), postsynaptic protein Homer1 (Rabbit, polyclonal, Recombinant protein of human homer (aa1-186), Synaptic Systems, 160003, AB_887730, dilution 1:500), glial glutamate transporter GLT-1 (Guinea pig, Polyclonal, Synthetic peptide from the C-terminus of rat GLT-1, Merck, AB1783, AB_90949, dilution 1:500). Secondary antibodies were: anti-mouse IgG (Donkey, CF568-conjugated, Biotium, 20105, AB_10557030, dilution 1:500), anti-rabbit IgG (Goat, Atto488-conjugated,

Rockland, 611-152-122S, AB_10893832, dilution: 1:500), anti-guinea pig IgG (Donkey, Alexa647-conjugated, Jackson ImmunoResearch Labs, 706-606-148, AB_2340477, dilution: 1:500).

To obtain spatial patterns of individual proteins in the synaptic microenvironment, we employed the single-molecule localization microcopy (SMLM) technique direct stochastic optical reconstruction microscopy (dSTORM) (Endesfelder and Heilemann, 2015) . Images were recorded with a Vutara 350 microscope (Bruker). The targets were imaged using 640 nm (for Alexa647), 561 nm (for CF568) or 488 nm (for Atto488) excitation lasers and a 405 nm activation laser. We used a photoswitching buffer containing 100 mM cysteamine and oxygen scavengers (glucose oxidase and catalase) (Metcalf et al., 2013). Images were recorded using a 60x-magnification, 1.2-NA water immersion objective (Olympus) and a Flash 4.0 sCMOS camera (Hamatasu) with frame rate at 50 Hz. Total number of frames acquired per channel ranged from 5000-20000. Data were analyzed using the Vutara SRX software (version 6.02.05) and a custom-written script for MATLAB. Single molecules were identified by their continued emission frame-by-frame after removing the background. Identified particles were then localized in three dimensions by fitting the raw data with a 3D model function, which was obtained from recorded bead data sets. The experimentally achievable image resolution is 20 nm in the *x*-*y* plane and 50 nm in the *z* direction; in tissue sections we routinely achieved *x*-*y* resolution of 58.0 ± 7.1 and *z*-resolution of 73 ± 5.8 nm.

Chemical induction of long-term potentiation

The classical 'chemical' LTP (cLTP) was induced by perfusing the acute slice for 10-15 min with the Mg-free ACSF solution containing 4 mM $CaCl_2$ (Sigma), 0.1 µM rolipram (Cayman Chemical Company), 50 µM forskolin (Cayman Chemical Company) and 50 µM picrotoxin (Sigma) (Otmakhov et al., 2004). This treatment increases the level of cAMP and that of network activity leading to a tetanic-like stimulation in bulk that potentiates the majority of excitatory synapses.

LTP induction by two-photon spot-uncaging of glutamate

We used a combined two-photon uncaging and imaging microscope (Olympus, FV-1000MPE) powered by two Ti:Sapphire pulsed lasers (Chameleon, Coherent, tuned to 720 nm for uncaging and MaiTai, Spectra Physics, tuned to 840 nm for imaging). The intensity of the imaging and uncaging laser beams under the objective was set to 5 mW and 12-17 mW, respectively. CA1 pyramidal neurons and astrocytes were loaded with Fluo-4 (200 µM) and Alexa Fluor 594 (100 µM) and held in current-clamp mode. The MNI-glutamate was applied in the bath at 2.5 mM. The stimulation protocol was delivered >30 µm from the cell soma and included three series of 100 x 1ms pulses at 100Hz, 60 seconds apart. The uncaging spot was placed ~1µm from the identifiable small process in astrocytes or the dendritic spine head in patched and visualized CA1 pyramidal neurons.

To test whether this protocol elicited LTP, CA1 pyramidal neurons were recorded in whole-cell patch clamp (see above), and EPSCs were elicited by 1 ms uncaging pulses delivered every 3 min. After a 10 min baseline, the neuron was held in current clamp (-60 to -65 mV, as in freely-moving rats (Epsztein et al., 2010)) and LTP was induced using the glutamate uncaging protocol. Once the induction protocol had been completed, EPSCs were monitored in voltage clamp for 30 min.

For IP_3 uncaging, 400 µM NPE-caged IP_3 (D-Myo-Inositol 1,4,5-Triphosphate, P4(5)-(1-(2-Nitrophenyl)ethyl) ester, Life Technologies) were added to the internal solution. The uncaging protocol consisted of 3-5 cycles (200 ms apart) of 5-10 ms pulses on 4-5 points, repeated 3 times every 60 s. To test the effect of glutamate and IP_3 uncaging on astrocyte morphology, astrocytes located in the *stratum radiatum* of CA1 were loaded with Fluo-4 (200 µM) and Alexa Fluor 594 (100 µM).

In baseline conditions and 30-40 min after the glutamate-uncaging LTP induction protocol, Z-stacks of the same region of the astrocyte were collected every 60-120 seconds. The intracellular Ca^{2+} response to glutamate and IP_3 uncaging was recorded using frame-scans in astrocytes (Figs. 4A, 5E) and linescan recordings in dendritic spines of CA1 pyramidal cells and expressed as $\Delta G/R$ values (green/red ratio; Fluo-4 fluorescence normalized to the Alexa Fluor 594 signal, Fig. S5A-B).

Probing ephrins and extracellular matrix signaling

The candidate morphogenic signals that could be invoked during LTP induction involve signaling molecules of the extracellular matrix (ECM) (Dityatev and Rusakov, 2011) or the ephrin/Eph-dependent neuron-astrocyte signaling attributed to astrocyte-dependent stabilization of newly formed dendritic protrusions (Nishida and Okabe, 2007). The protocol for catalytic removal of chondroitin sulfate (and side chains of proteoglycans) with Chondroitinase ABC (0.5U/ml, 45 min, 33ºC) has been established and validated by us previously (Kochlamazashvili et al., 2010). Similarly, the blockade of EphA4 activity with EphA4-Fc (10 µg/ml) using previously tested protocols was carried out in accord with the reported procedures (Murai et al., 2003). Because degrading the ECM's hyaluronic acid with hyaluronidases interfered with LTP induction (Kochlamazashvili et al., 2010) such experiments were not included in the present study. Suppressing NKCC1 activity in the recorded astrocyte was performed through intracellular dialysis of bumetanide (20 µM) (Migliati et al., 2009).

Monitoring extracellular glutamate transients with optical glutamate sensors

We modified FLIPE600n (Okumoto et al., 2005) to contain a biotin tag for immobilization of the sensor in the tissue, as described previously (Whitfield et al., 2015). A nucleotide sequence coding for the biotin tag was synthetized de novo (Epoch Life Science), amplified using PCR and then inserted into pRSET FLIPE-600n (Addgene #13537, courtesy of Wolf B. Frommer) using BamHI restriction site.

bFLIPE600n reports glutamate levels through a FRET mechanism, by changing the fluorescence intensity ratio R = ECFP/Venus. Calibration of the bFLIPE600n sensor using 2PE was first done in free solution (Fig. S5A-B). bFLIPE600n in PBS (3-4 µM, pH 7.4) was placed in a meniscus under the microscope objective. Increasing amounts of glutamate (dissolved in PBS, pH adjusted to 7.4) were added and changes in the ECFP/Venus emission ratio were calculated offline. For experiments in acute slices, 30-40 µM bFLIPE600n were preincubated with 5-7 µM streptavidin in PBS at 4° C for at least 12 h. A standard patch pipette (2-4 MΩ resistance) was then backfilled with the sensor solution and bFLIPE600n was gently injected into the CA1 s. *radiatum* of biotinylated slices (see above and (Whitfield et al., 2015)) at 70-100 µm depth applying light positive pressure for 10-20 s. Sensor levels were allowed to equilibrate for 15 min before recordings started at a depth of 50-60 µm below the slice surface (~3 mW excitation intensity at the focal plane). Schaffer collateral stimulation was done as described above except that the stimulation intensity was ~50% of the one inducing near-maximal fEPSP responses.

Evaluating the extent of extracellular glutamate transients with iGluSnFR

iGluSnFR was expressed in the CA1 region of the hippocampus as described above. A iGluSnFR-expressing CA1 pyramidal neuron was loaded with 100 µM Alexa Fluor 594 to visualize dendritic spines. The iGluSnFR fluorescence was monitored in linescan mode (λ_x^{2P} = 910 nm, 500 Hz) following MNI-glutamate uncaging (1 ms pulse, 2.5 mM in the bath). The linescan was positioned near the closest dendritic spines head, parallel to the dendritic stem (Fig. 6D). In baseline conditions, three linescan images were recorded 3 min apart and averaged (Fig. 6E, top). LTP was induced with 2PE uncaging of glutamate as described above. 5-10 min following LTP induction, five linescan images were recorded every five minutes for averaging (Fig. 6E, bottom).

In each linescan image, two ~30 ms long ROI bands were selected for analyses, one shortly before the spot-uncaging onset (background iGluSnFR fluorescence profile F_0 along the linescan axis x, $F_0(x,t)$) the and one ~10 ms after (glutamate-bound iGluSnFR profile $F(x,t)$; Fig. 6E). The pixel brightness values (originally recorded grey scale) in these iGluSnFR linescan images were (i) averaged along the timeline t, and (ii) among the pre-uncaging and the post-uncaging groups in each trial, thus giving average profiles $F^*_0(x)$ and $F^*(x)$, respectively, for trials before and after LTP induction. In each trial therefore the glutamate signal profile was obtained as a pixel-by-pixel image (vector) operation $(F^*(x)-F^*_0(x)) / F^*_0(x)$ giving the glutamate-bound iGluSnFR brightness distribution $\Delta F/F_0\,(x)$ along a linescan axis near the uncaging spot. The distribution $\Delta F/F_0\,(x)$ along x-axis (distance) was best-fit approximated with a Gaussian centered at the uncaging spot, with the amplitude A and dispersion σ being free parameters (OriginPro, Origin Lab Corp, MA).

Evaluating NMDAR-mediated inter-synaptic cross-talk in a two-pathway experiment

The NMDAR-mediated synaptic cross-talk was probed by taking advantage of the use-dependency of the NMDAR inhibitor MK801, as described in detail earlier (Scimemi et al., 2004). CA1 pyramidal cells where held in voltage clamp to record EPSCs in response to stimulation of two independent synaptic CA3-CA1 pathways (see Fig. 4c for an illustration, GABA receptors blocked as described above). While individual pathways displayed a robust (same-pathway) paired-pulse facilitation of 75.4 ± 6.1% (n = 54, $P < 0.001$; inter-stimulus interval 50 ms), the facilitation was approximately five times lower between the pathways (16.5 ± 2.9%, $P < 0.0001$) thus indicating that these pathways do not interact presynaptically by more than ~20%. Separation of pathways was helped by making an additional cut into the *stratum radiatum* in parallel to the pyramidal cell layer. AMPAR-mediated EPSCs were recorded at a holding potential of -70 mV for 10-15 minutes. In a subset of experiments LTP was induced on one or both pathways (HFS, see above). NMDAR-mediated EPSCs of the same pathways were then recorded by clamping the cell to -20 mV and inhibiting AMPAR with 10 µM NBQX. MK801 (4 µM) was bath-applied after another baseline period. Stimulation of the test pathway was then stopped and resumed after 20 minutes. EPSCs were evoked at 0.1 Hz throughout the experiment. Synaptic cross-talk was quantified at the test pathway by calculating the reduction of NMDAR-mediated EPSC amplitudes in the absence of test pathway stimulation relative to baseline.

An LTP-associated increase of the presynaptic release probability (PR) may facilitate cross-talk independent of astrocyte morphology changes. According to the binomial model of release, an increase of PR would decrease the variability of postsynaptic responses (coefficient of variation [CV]). Experiments using LTP induction in a single pathway showed that the CVs for the baseline AMPAR and NMDAR-mediated responses were not different between pathways

and within a pathway ($1/CV^2$, four paired Student t-tests, $p > 0.18$). In addition, the rate of blockade of NMDAR-mediated response by MK801 is an indicator PR and was not affected by LTP-induction (Fig. S6G).

Recordings were carried out using a Multiclamp 700B (Molecular Devices). Signals were filtered at 3-10 kHz, digitized and sampled through an AD converter (National Instruments or Molecular Devices) at 10-20 kHz, and stored for off-line analysis using pClamp10 software (Molecular Devices). Receptor blockers were purchased from Tocris and Abcam Biochemicals.

Monte Carlo simulations

Monte Carlo simulations of glutamate diffusion, uptake and NMDAR activation in the environment of the CA3-CA1 synapse. The modelling approach was described and validated against experimental data previously (Savtchenko et al., 2013; Zheng et al., 2015; Zheng et al., 2008). In brief, the presynaptic part (Schaffer collateral en-passant boutons) and the postsynaptic part (dendritic spine heads of CA1 pyramidal cells) were represented by the two truncated hemispheres separated by a 300 nm wide 20 nm high apposition zone including a 200 nm wide synaptic cleft (Fig. S7), to reflect the typical three-dimensional ultrastructure reported for these synapses (Harris et al., 1992; Lehre and Rusakov, 2002; Shepherd and Harris, 1998; Ventura and Harris, 1999). The synapse was surrounded by 20-30 nm wide extracellular gaps giving an extracellular space fraction $\alpha \sim 0.15$. 3000 molecules of glutamate (Savtchenko et al., 2013) were released at the cleft center and allowed to diffuse freely. The diffusion coefficient for glutamate (excluding space tortuosity due to cellular obstacles) was set at 0.4 $\mu m^2/ms$ (Zheng et al., 2008). The statistics on activation of extrasynaptic NMDARs were collected using a cluster of receptors placed at 200-250 nm from the synaptic centroid (thus approximately equidistant to the two nearest-neighboring synapses in area CA1 (Rusakov and Kullmann, 1998)). To test four different scenarios pertinent to the astroglial environment of synapses, we distributed glial glutamate transporters (EAAT1-2 type) using four different patterns that occupy four sectors of the extrasynaptic environment (Fig. S7). In the control case (baseline conditions) their extracellular density was ~0.2 mM, to match a membrane surface density of $5\text{-}10 \bullet 10^3$ μm^{-2} (Lehre and Danbolt, 1998) reported earlier. Cases (*i*-*iii*) thus mimicked possible astroglial re-arrangements following LTP induction. In case (*i*), the transporter density doubled while the astrocyte membrane area occupied by them was reduced two-fold (thus the total transporter number was unchanged); case (*ii*) was similar to (*i*) but with the transporter density unchanged (total number was reduced two-fold); and in the case (*iii*) the transporter-occupied area was rearranged towards one side of the nearby NMDAR cluster. During extensive control simulations we found no interaction between any of the four sectors in terms of transporter or NMDAR activation by released glutamate. In our tests therefore we could compare the four scenarios using the same simulations run (repeated 32 times for a statistical assessment of the stochastic receptor and transporter actions). Our simulations have suggested that, somewhat paradoxically, one factor that could prolong the presence of glutamate near NMDARs and therefore boosting receptor activation could be its stochastic unbinding from local transporters, as suggested earlier (Rusakov, 2001). Simulations were carried out using a dedicated 14-node PC cluster running under Linux (Zheng et al., 2015).

Quantification and statistical analysis

The present study contained no longitudinal or multifactorial experimental designs. In electrophysiological or imaging experiments the main source of biological variance was either individual cells or individual preparations (the latter in case of field measurements in acute slices), as indicated. In accord with established practice, in the *ex vivo* tests we routinely used

one cell per slice per animal, which thus constituted equivalent statistical units in the context of sampling, unless indicated otherwise. Statistical hypotheses pertinent to mean comparisons were tested using a standard two-tailed *t*-test, unless the sample showed a significant deviation from Normality, in which case non-parametric tests were used as indicated. The null-hypothesis rejection-level was set at $\alpha = 0.05$, and the statistical power was monitored to ensure that that the sample size and the population variance were adequate to detect a mean difference (in two-sample comparisons) of 10-15% or less. Group data are routinely reported as mean ± s.e.m., unless indicated otherwise, and the statistical difference between the population averages was estimated using the *t*-test (for paired or independent samples). Two-tailed tests were routinely used, and sample pairing was used where appropriate, e.g., when monitoring real-time changes in a parameter against its baseline value or when comparing cells in paired recordings.